

Compression behavior of individual thin-walled metallic hollow spheres with patterned distributions of microporosity

Jinliang Song^{a,b}, Quansheng Sun^a, Shengmin Luo^b, Sanjay R. Arwade^b, Simos Gerasimidis^b, Yi Guo^c, Guoping Zhang^{b,*}

^a Department of Civil Engineering, Northeast Forestry University, Harbin 150040, China

^b Department of Civil and Environmental Engineering, University of Massachusetts Amherst, Amherst, MA 01003, USA

^c Diamond Offshore Drilling, Inc., Houston, TX 77094, USA

ARTICLE INFO

Keywords:

Compression testing
Failure mode
Finite element method
Metallic hollow sphere
Nanoindentation
Porous material

ABSTRACT

This paper presents an integrated experimental and computational study of the compression behavior of individual thin-walled metallic hollow spheres (MHS) with patterned distributions of microporosity. Quasi-static compression testing, including purely elastic loading, was conducted on two groups of individual MHS with two different sizes to examine the entire deformation process as well as the purely elastic response. Three-dimensional finite element modeling was then performed to investigate the effects of different microporosity distribution patterns on the MHS compression behavior and to understand the pertinent deformation and failure mechanisms. Results show that the Young's modulus and collapse stress of individual MHS with a uniform microporosity distribution decrease nonlinearly with porosity, which follows the same power-law functions developed for the porous wall material. For other patterned (i.e., vertical, horizontal, and random) distributions of microporosity involving localized weak wall sections, buckling commences at the weak sections, generating “buckling lines”, followed by buckling failure along these adjacent or converged “buckling lines”. Moreover, among the “buckling lines” generate some hinges that contribute to the increased load-bearing capability during the densification process. These findings can shed lights on the design, manufacturing, and modeling of individual MHS and MHS-based materials with specifically tailored engineering performance.

1. Introduction

Metallic hollow sphere (MHS) structures (MHSS) are becoming increasingly attractive for many applications ranging from aerospace materials (e.g., sandwich panels), to industrial functionalities (e.g., energy-absorbing and damping structures), and to medical replacements (e.g., biomedical artificial limbs) [1], mostly owing to their high strength and extremely low density. To date, several novel technologies have been developed that manufacture MHS with a wide range of diameters (D) and wall thickness (t), such as coating styro-foam using fluidized bed powder metallurgy or electrodeposition processes, and coreless methods using inert gas atomization of metallic alloys [2]. MHSS are typically made of numerous MHS attached together by sintering, soldering, or epoxy resin, among others, and the configuration and arrangement of spheres in MHSS can be divided into five sub-groups: simple cubic (SC), body-centered cubic (BCC), face-centered cubic (FCC), hexagonal-closed packing (HCP), and random packing [3]. The majority of publications aims to understand the mechanical

properties of MHSS by studying their compressive, tensile, fatigue, and dynamic behavior [4–10]. In general, the mechanical properties of MHSS are dominantly dictated by the characteristics of individual MHS, inter-sphere bonding, and packing configurations. Therefore, the mechanical behavior of individual MHS is of fundamental importance to the understanding of the mechanical performance of MHSS. However, the MHS are characterized by a high microporosity within the porous thin wall. As a result, the dependence of the mechanical (including elastic, plastic, collapsing, and buckling) behavior of individual MHS upon the porosity and its distribution is worth further investigation.

A number of experimental, numerical, and analytical studies have been reported on the quasi-static compression behavior of individual hollow spheres. Lim studied the deformation behavior of the 405 ferritic stainless steel hollow spheres (with $D = 2$ mm and $t/D = 0.05$) and found that the deformation process is significantly controlled by plastic bending and, upon densification, wall contacts [4]. Carlisle et al. experimentally measured and parametrically simulated the uniaxial compression behavior of carbon microballoons ($D = 22\mu\text{m}$ and a

* Corresponding author.

E-mail addresses: zhangg@umass.edu, gzhang@alum.mit.edu (G. Zhang).

<https://doi.org/10.1016/j.msea.2018.08.016>

Received 2 May 2018; Received in revised form 18 July 2018; Accepted 6 August 2018

Available online 08 August 2018

0921-5093/ © 2018 Elsevier B.V. All rights reserved.

relatively larger $t/D = \sim 0.06\text{--}0.1$ [11,12]. Gupta et al. extended the investigation of quasi-static compression of large hollow aluminum spheres ($D = 40\text{--}125$ mm with a mixed range of $t/D = 0.002\text{--}0.03$) to compression at high loading rates of up to 10 m/s [13–15]. Besides, several papers have reported the dynamic behavior of hollow spheres. Ruan et al. reported the crushing behavior of a single ping-pong ball compressed by point loading, rigid ball, rigid plate, rigid cap, and double rigid balls, as well as the one-dimensional (1D) and 2D load-deformation behavior compressed by rigid plates [6]; Dong et al. studied the collapse behavior of selected ping-pong ball arrays under different impact velocities using a split Hopkinson pressure bar (SHPB) system [16]; Li et al. conducted high loading-rate experiments and finite element modeling (FEM) to investigate the underlying deformation and failure mechanisms of thin-walled hollow nickel spheres [17]. On the other hand, these experimental, computational, and analytical studies focusing on the quasi-static or dynamic behavior of hollow spheres usually consider the thin wall as a nonporous and homogeneous material, especially in the FEM simulations. In reality, some thin-walled hollow spheres such as ping-pong balls have highly uniform sizes and shape but a very small discrepancy in wall thickness. However, the thin wall of most real manufactured MHS has a high to very high porosity due to their unique metallurgical manufacturing process. Moreover, most pores within the thin wall are irregular polygons in shape. In fact, the MHS thin wall is a kind of highly porous material. For porous materials, several approaches have been developed concerning the relationship between their mechanical properties and porosity. For example, Roberts and Garboczi et al. used FEM to study the influence of porosity and pore shape on the elastic properties of some porous ceramics, and established three types of models to assess the dependence of elastic modulus and Poisson's ratio on porosity: overlapping solid spheres, overlapping spherical pores, and overlapping ellipsoidal pores [18]; Song et al. conducted nanoindentation testing and synchrotron X-ray computed tomography (XCT) to characterize the mechanical properties and microstructure of porous MHS thin walls respectively, then used the real microstructure obtained by XCT to build the physical FEM models for simulation, and further developed the nonlinear relationships linking the Young's modulus and yield strength of the porous thin wall to its porosity, with the exact formulae for estimating the mechanical properties of the porous thin wall based on the real pore morphology and microstructure [19].

With regard to the research methods, in addition to experimental investigations, FEM has been widely used to simulate the macroscopic response of individual MHS and MHSS under quasi-static or dynamic compression [20,21], and even to probe the buckling and post-buckling behavior of thin-walled shells [22–24]. In these work, one of the basic assumptions is that the thin wall of MHS is a nonporous and homogeneous material. However, the actual manufactured MHS always have such features as varied wall thickness and differently-sized micropores within the thin wall. In other words, there is a discrepancy between the ideal MHS considered in computational and analytical studies and the real manufactured ones used in practice. Therefore, it is necessary and important to understand the actual deformation and failure behavior of the manufactured MHS. One particular advantage of FEM modeling is that insights into the physical mechanisms underlying the phenomenological behavior of thin-walled MHS with different microporosities can be elucidated, and hence FEM can be used to investigate and analyze the compression process and failure of individual MHS with differently patterned distributions of microporosity, prior to the development of viable technologies for manufacturing MHS and MHSS with controlled microporosity and specifically tailored mechanical functionalities.

Although the deformation and failure process of ideal MHS with the so-assumed nonporous and homogeneous thin wall have been discussed in the literature, little effort has been made to study the properties of those manufactured ones with varied microporosity and wall thickness distributions. This paper aims to fill this gap with an integrated experimental and computational study: while experimental work mainly

involves the quasi-static compression, including purely elastic loading, of manufactured individual MHS with real but unknown microporosity to understand their deformation process, computational work consists of FEM modeling to fully investigate the underlying mechanisms for quasi-static deformation and failure that make up the overall constitutive behavior of MHS with differently patterned distributions of microporosity. Results from the experimental measurements and FEM simulations will be compared and then exploited to assess the microporosity and its distribution of the manufactured MHS. Findings can expectedly advance the design and manufacturing of individual MHS and MHS-based foam materials as well as the modeling and prediction of their mechanical performance.

2. Materials and methods

2.1. Materials

The studied MHS, manufactured by the Fraunhofer Institute for Advanced Materials (Dresden, Germany), were selected from the same batch of samples studied by Song et al. [19]. The diameter, wall thickness, and wall porosity of these hollow spheres are slightly different from each another, and the two most common diameters are ~ 2 and ~ 3 mm with a wall thickness ranging from 0.01 to 0.04 mm. Interestingly, preliminary microscopic observations found that the MHS with relatively larger diameters have thinner walls (i.e., $D = \sim 3$ mm with an average $t = 0.02$ mm) than those smaller spheres (i.e., $D = \sim 2$ mm with an average $t = 0.03$ mm). The MHS wall is made of medium carbon steel with a Young's modulus of 207 GPa and a yield strength of 982 MPa, as measured by prior nanoindentation testing [19]. Images obtained by a scanning electron microscope (SEM, FEI Inc., Hillsboro, OR, USA) clearly reveal that the MHS wall possesses randomly distributed, multiscale pores with complex morphologies and pore sizes of 1–2 to ~ 50 μm (Fig. 1). Synchrotron XCT [19] indicates that the microporosity of the MHS wall varies from $\sim 5\%$ in some local sections to as high as $\sim 42\%$ for an entire cross-sectional surface (Fig. 2).

2.2. Quasi-static compression testing

To characterize the entire compression process of individual MHS, unidirectional, quasi-static compression testing was conducted on eight randomly selected MHS with carefully measured diameters (i.e., $D = 2.905, 2.910, 2.945, 2.968, 1.987, 1.994, 2.009, 2.012$ mm), which were divided into two subgroups based on their diameters: $D = \sim 2$ or ~ 3 mm. Each MHS was first cleaned with ethanol to remove dust and other potential contaminants on its surface, and then subjected to unidirectional compression testing between two smooth stainless steel platens in a GeoJac loading system (Trautwein Soil Testing Equipment, Inc., Houston, TX) at a displacement rate of 0.05 mm/min in the ambient laboratory environment (i.e., at a room temperature of ~ 25 $^{\circ}\text{C}$). The nominal strain ε and nominal stress σ representing the measured engineering strain and stress are defined as the vertical deformation δ and load P normalized by the diameter and external cross-sectional area of the MHS, respectively, which are given as [25]:

$$\varepsilon = \frac{\delta}{D} \quad (1)$$

$$\sigma = \frac{P}{S} = \frac{4P}{\pi D^2} \quad (2)$$

where S is the external diameter-based overall cross-sectional area of the sphere.

Since the individual MHS was compressed unidirectionally (i.e., with 2 contacting points) without any lateral confinement, the horizontal deformation was not explicitly considered. Moreover, the horizontal deformation is nonuniform along the vertical direction, making it difficult to measure and quantify this parameter. Nevertheless, the

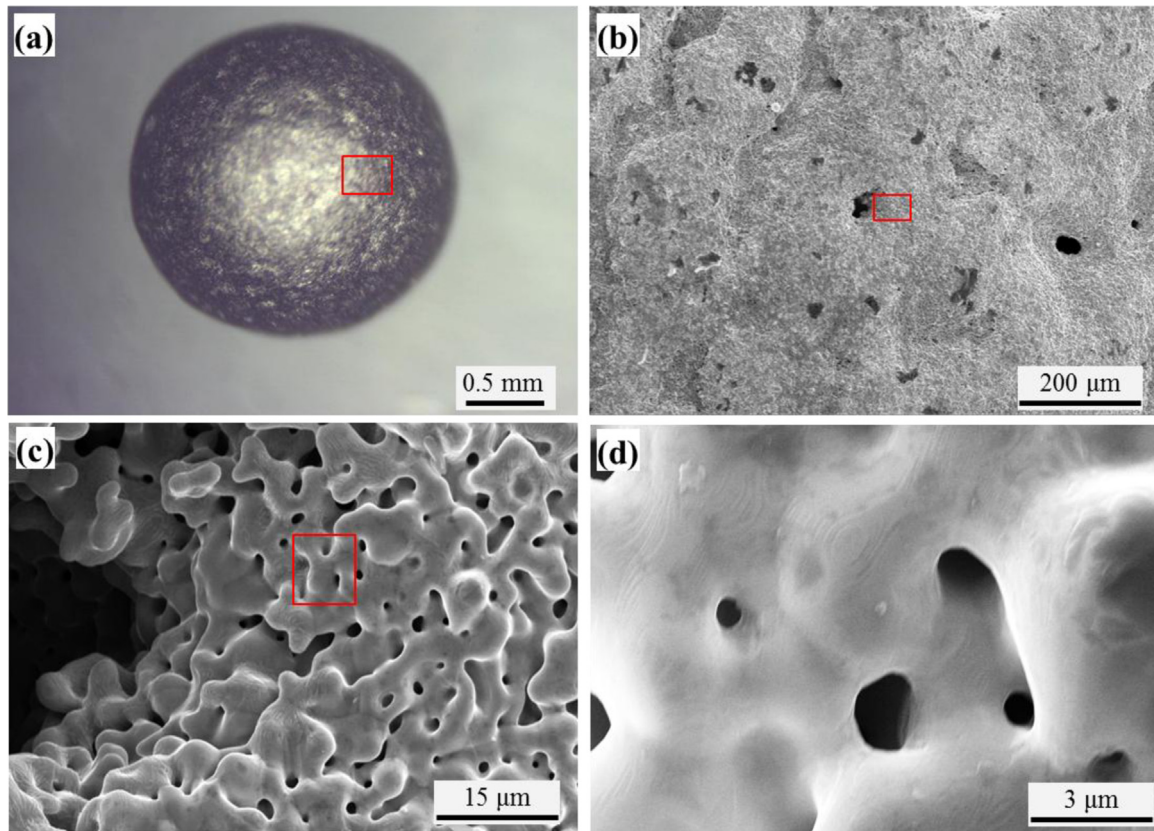


Fig. 1. The morphology of porous thin wall of MHS observed under a scanning electron microscope (SEM): (a) a MHS showing the imperfections and the SEM scanning spot on its external surface; (b), (c), and (d) SEM micrographs showing differently-sized pore morphology of the MHS thin wall at different scales.

horizontal deformation will be considered in future work where an MHS is compressed with multiple (i.e., > 2) points of contact.

2.3. Purely elastic compression testing

The aforementioned compression testing can capture the entire deformation process of individual MHS, but is incapable of precisely characterizing their elastic deformation, owing to the relatively low resolutions of the conventional load cell and displacement transducers used in the loading system. Therefore, purely elastic, unidirectional compression testing was also conducted in a Keysight G200 nanoindenter (Keysight Technologies, Inc., USA) at the ambient laboratory conditions. A cylindrical diamond punch with a smooth flat end of 1.0 mm in diameter instead of a sharp indenter tip was used as the top platen, while a polished sapphire sheet with dimensions of $10 \times 10 \times 0.5$ mm was glued onto an aluminum puck to serve as the smooth bottom platen. The nanoindenter has a maximum load capacity of 500 mN with a resolution of 50 nN and a maximum displacement of $\pm 750 \mu\text{m}$ with a resolution of < 0.01 nm. The purely elastic compression, including loading-unloading cycles, was conducted under the load control mode on two carefully selected MHS with outside diameters of 2.968 and 1.994 mm, respectively. The loading-unloading cycle used a constant loading rate of 13.33 mN/s and a maximum load of 200 mN. The corresponding vertical displacements were measured to be < 3000 nm (as discussed later). The Hertz elastic contact theory was used to analyze the experimental data [26]. The reduced modulus E^* of the MHS-platen contacts and the Young's modulus of the MHS (i.e., as a thin-shelled structure), but not the porous thin wall material, was determined by the following equations:

$$E^* = \frac{3P}{(D\delta^3)^{0.5}} \quad (3)$$

$$\frac{1}{E^*} = \frac{1 - \nu_1^2}{E_1} + \frac{1 - \nu_2^2}{E_2} \quad (4)$$

where ν_1 and ν_2 are the Poisson's ratios of the MHS and platens; E_1 and E_2 the Young's modulus of the MHS and platens, respectively; For diamond, $E_2 = 1141$ GPa, $\nu_2 = 0.07$ [27,28]; For the MHS, ν_1 is taken as 0.3 [29]. Because both diamond and sapphire are much harder and stiffer than the MHS, the MHS-diamond contact can behave very similar to the MHS-sapphire contact.

2.4. Finite element modeling

To understand the deformation process of the MHS with varied microporosity distribution patterns and pertinent evolution of stress distributions, FEM modeling was performed in a commercial platform, ABAQUS v.6.10 (Dassault Systèmes Americas Corp., Waltham, MA, USA). A 3D hollow sphere model was first established using the S4R shell element as the basic element type (Fig. 3a), and five different porosity distribution patterns were independently applied to this model, including uniform distribution of microporosity (UDM), vertical distribution of microporosity (VDM), horizontal distribution of microporosity (HDM), random distribution of microporosity (RDM), and random distribution of wall thickness and microporosity (RDTM) (Fig. 3b-d). In addition, for each type of the microporosity distribution pattern, two different diameters and wall thicknesses, i.e., $D = 2$ mm and $t = 30 \mu\text{m}$ as well as $D = 3$ mm and $t = 20 \mu\text{m}$, were also applied to the FEM model, so that the results from computational simulations were comparable with the experimental ones.

Table 1 summarizes all simulated MHS FEM models with their characteristics. For the MHS with UDM, totally eight MHS, each with a constant wall thickness and a constant, uniformly distributed porosity that varies from 0% to 32.88%, were considered. For the MHS with VDM, the sphere was segmented into 16 vertical sections that were

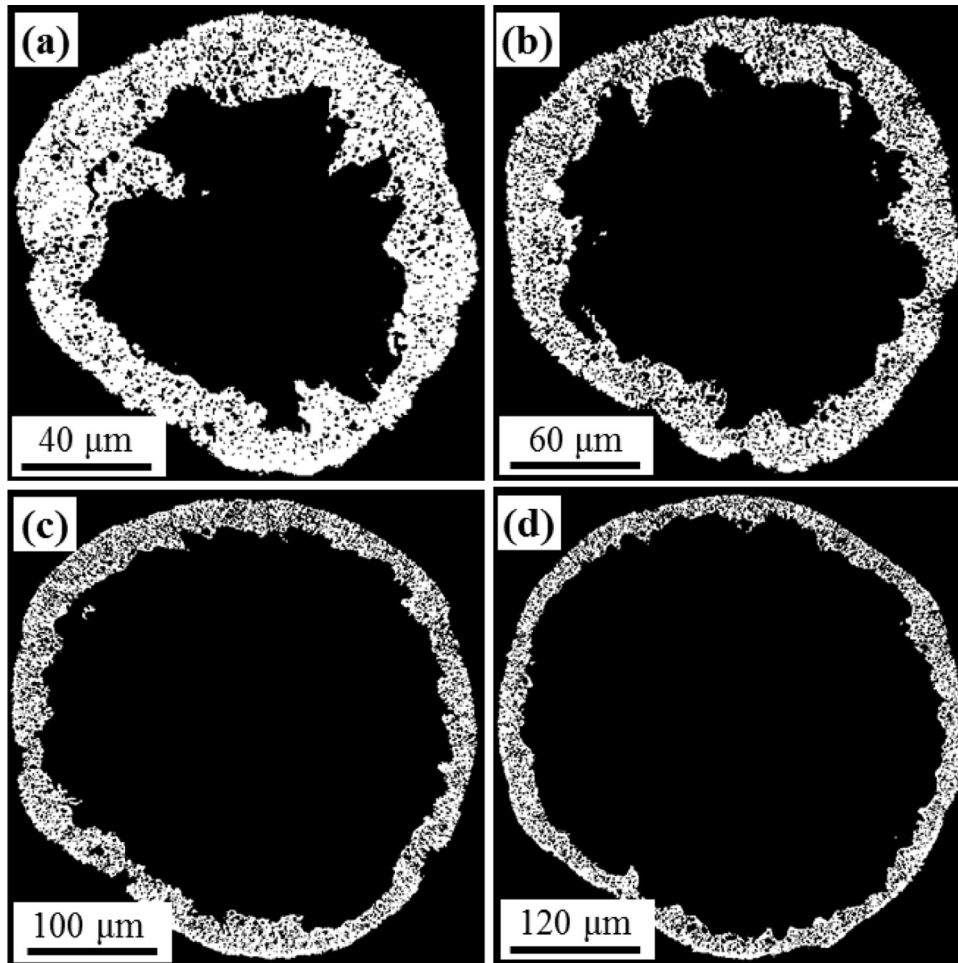


Fig. 2. Synchrotron X-ray computed tomography (XCT) slice images showing the geometry of the MHS cross-sections and pore morphology of the MHS thin wall.

further segmented along the equator into two parts, resulting in a total of 32 sections. Each section was then assigned a porosity randomly selected from the 8 values ranging from 0% to 32.88% (Fig. 3b). For the MHS with HDM, the sphere was segmented horizontally into 10 sections, each with an assigned porosity ranging from 0% to 32.88%. For the MHS with RDM, the model was divided into 32 vertical and 20 horizontal slices, leading to much smaller sections (i.e., a total of 640 sections); each section was then randomly assigned a porosity selected from the 8 values ranging from 0% to 32.88%. For the RDTM, each small section was also randomly assigned a wall thickness varying from 0.01 to 0.04 mm (Table 1).

For all simulations, the explicit ABAQUS solver was used to simulate the quasi-static compression response of individual MHS. A deformable MHS was placed between two rigid and smooth end platens, with the bottom one as a fixed boundary and the top one as a loading punch. All degrees of freedom of the two end platens were constrained except the vertical displacement of the top one, so that the compression was applied along the vertical direction via a displacement-controlled mode.

The plastic behavior of many pure and alloyed metallic materials can be closely approximated by a power-law equation, which can describe simple elasto-plastic, true stress-true strain behavior as follows [30]:

$$\sigma = \begin{cases} E\varepsilon, & \text{for } \sigma \leq \sigma_y \\ R\varepsilon^n, & \text{for } \sigma \geq \sigma_y \end{cases} \quad (5)$$

where E is the Young's modulus of the metallic material, σ_y the initial yield strength, ε_y the corresponding yield strain, n the strain hardening exponent, and R a strength coefficient. Thus,

$$\sigma_y = E\varepsilon_y = R\varepsilon_y^n \quad (6)$$

The yield strength σ_y is defined at the zero offset or plastic strain, and the total effective strain ε consists of two parts, ε_y and ε_p ,

$$\varepsilon = \varepsilon_y + \varepsilon_p \quad (7)$$

where ε_p is the nonlinear part of the total effective strain accumulated beyond ε_y , or the purely plastic strain. With Eqs. (6) and (7), when $\sigma > \sigma_y$, Eq. (5) becomes

$$\sigma = \sigma_y \left(1 + \frac{E}{\sigma_y} \varepsilon_p \right)^n \quad (8)$$

In this paper, the relationships among the Young's modulus E_w , the yield strength Y_w , and the microporosity Φ of the MHS porous thin wall material were taken from previous results presented in Song et al. [19]. The Poisson's ratio ν of the nonporous thin wall material was taken as 0.3, which was used to derive the Poisson's ratio ν_w for the porous thin wall material by following the method developed by Roberts and Garboczi [18]. The strain hardening exponent n was taken as 0.2, and a total effective strain ε of 0.2 was adopted. A contact element approach was used with plenty formulations on interpenetration, and the friction coefficient between the MHS-end platen contact was taken as 0.1. To quantify and compare the macroscopic deformation of a single MHS, the nominal strain and stress were determined by Eqs. (1) and (2).

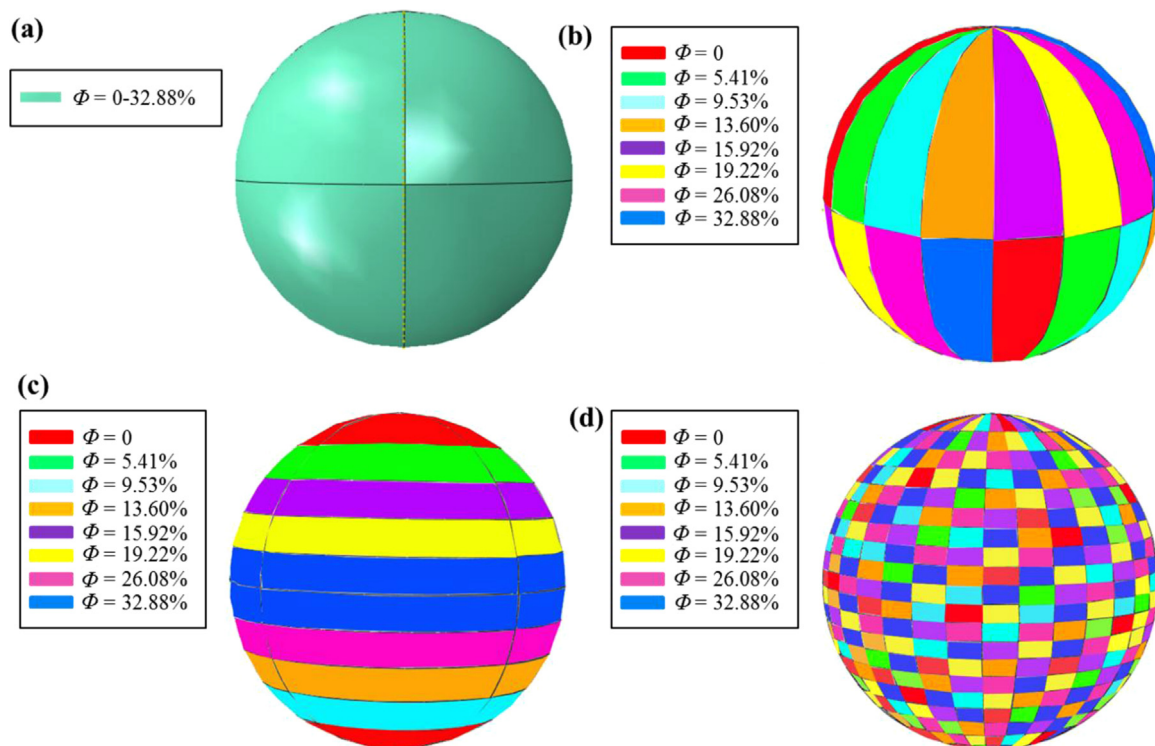


Fig. 3. Different models used for FEM simulations with various microporosity distribution patterns within the thin wall of individual MHS ($D = 3$ and 2 mm): (a) uniform distribution of microporosity (UDM); (b) vertical distribution of microporosity (VDM); (c) horizontal distribution of microporosity (HDM); (d) random distribution of microporosity (RDM) and random distribution of wall thickness and microporosity (RDTM).

3. Results and discussion

3.1. Quasi-static compression testing

The nominal stress-strain curves obtained from the unidirectional compression tests are shown in Fig. 4a and b for the two groups of MHS with $D = \sim 3$ and ~ 2 mm, respectively. In general, similar stress-strain and deformation features are observed for the two groups of MHS, although their diameters and thicknesses are different. However, the $D = \sim 2$ mm MHS with a higher t/D ratio exhibit stronger resistance to compression than the other group, and their nominal stress-strain curves are more scattered throughout the entire process of compression. The former discrepancy obviously results from the higher t/D of the smaller MHS group, while the latter may possibly be caused by the higher variation in the random distribution of microporosity and in the nonuniform wall thickness of the $D = \sim 2$ mm MHS [19]. During compression, the weaker zones generally buckle first and generate larger deformation, and hence the nominal strain can be as high as 0.8–0.9. For both MHS groups, three distinct stages of deformation can be observed in the nominal stress-strain curves:

- Stage I ($\delta/D = 0$ –0.5): buckling and yielding. The nominal stress σ increases nearly linearly with increasing the nominal strain ϵ at this stage. All curves show some small-scale local serrations, implying that an MHS continuously experiences multiple local buckling and yielding in its thin wall. In addition, a very short, purely elastic section should exist at the onset of compression, but it is not readily discerned in the curves, again owing to the limited resolutions of the transducers used in the loading system.
- Stage II ($\delta/D = 0.5$ –0.8): collapse. The nominal stress σ slightly decreases with the nominal strain ϵ at this stage. Prior work found that the first self-contact of internal surface of the MHS wall occurs at this stage, which is mainly attributed to the gradual collapse of the MHS wall at various locations, especially around the two

contacting interfaces between the end platens and MHS. The collapse characterized by a decrease in the nominal stress σ results from the continuous local buckling failures that eventually merge together along a most likely horizontal wall section. Such a large area of yielding and buckling of course reduces the load-bearing capability of the MHS.

- Stage III ($\delta/D > 0.8$): self-densification. The nominal stress σ increases dramatically with the nominal strain ϵ at this stage. As the compression continues, the majority of the thin wall has collapsed and been densified, and the original spherical geometry of the MHS is finally compressed to a flat and thin configuration. Therefore, in this stage, large deformation leads to numerous self-contact points of the MHS internal surface, and the original large spherical thin shell is segmented into many small sections. This process is manifested by the rapid increase in the nominal stress σ even with a small increase in the nominal strain ϵ . At the end, the hollow chamber of the MHS nearly disappears and the stiffness is getting close to that of the bulk wall material.

Two sequences of snapshots of the quasi-static compression process for two individual MHS are shown in Fig. 5a & b as examples. Clearly, deformation commences from the two MHS-end platen contacting points. As a result, the sphere gradually changes to a drum-shaped configuration. Interestingly, it appears that little lateral deformation occurs during the initial compression stage (i.e., when $\delta/D < 0.2$). At the end of compression (i.e., when $\delta/D > 0.8$), both spheres transform to a flat, densified sheet.

3.2. Elastic properties of individual MHS

Fig. 4c shows the load-displacement curves of two selected MHS with $D = 2.968$ and 1.994 mm under purely elastic compression, and each curve involves a loading-unloading cycle. All curves are slightly concave-shaped and show nearly reversible deformation (i.e., the

Table 1
Summary of the five different microporosity distribution patterns used in the FEM models.

Distribution pattern	FEM Model	D (mm)	t (mm)	φ (%)	Characteristics of porosity distribution
Uniform (UDM)	UDM-MHS-1	3	0.02	0–32.88	The entire wall has the same thickness and a uniform porosity of 0–32.88%; Totally 8 models, each with a constant porosity, were simulated for each of the two MHS.
	UDM-MHS-2	2	0.03	0–32.88	
Vertical (VDM)	VDM-MHS-1	3	0.02	0–32.88	The MHS is cut into vertical sections, each with a different porosity selected from the eight values ranging from 0% to 32.88%.
	VDM-MHS-2	2	0.03	0–32.88	
Horizontal (HDM)	HDM-MHS-1	3	0.02	0–32.88	The MHS is cut into horizontal sections, each with a different porosity selected from the eight values ranging from 0% to 32.88%.
	HDM-MHS-2	2	0.03	0–32.88	
Random (RDM)	RDM-MHS-1	3	0.02	0–32.88	The MHS is cut into many small sections both horizontally and vertically, each with a different porosity randomly selected from 0% to 32.88%.
	RDM-MHS-2	2	0.03	0–32.88	
Random distribution of thickness & porosity (RDTM)	RDTM-MHS-1	3	0.01–0.04	0–32.88	The MHS is cut into many small sections both horizontally and vertically, each with a randomly selected porosity and wall thickness.
	RDTM-MHS-2	2	0.01–0.04	0–32.88	

loading-unloading hysteresis is nearly invisible). Noteworthy are the very small maximum load and displacement (i.e., ~ 200 mN and ~ 3000 nm) involved in the loading. The very small nominal strains (< ~ 0.15%), reversible loading and unloading curves, and completely recovered deformation demonstrate that nearly purely elastic, but no plastic, deformation occurs during the extremely low load compression. Based on the theory of Hertz elastic contact, Eq. (3) can be rewritten as:

$$3P/D^{1/2} = E^* \times \delta^{3/2} \tag{9}$$

To extract the reduced modulus of the MHS-end platen contacts, the loading-unloading curves in Fig. 4c are replotted in Fig. 4d with $3P/D^{1/2}$ and $\delta^{3/2}$ as the two axes. The linear fitting to the experimental data shown in Fig. 4d yields the reduced modulus E^* (i.e., the slopes of the two linear lines) as 8.33 and 9.13 GPa for the two tested MHS, respectively. According to Eq. (4), their Young's moduli are determined as 7.64 and 8.37 GPa, respectively. Since each MHS behaves as a thin-shelled structure, the larger MHS ($D = \sim 3$ mm) with a smaller t/D ratio of course exhibits a smaller Young's modulus than the smaller one with a larger t/D ratio. The elastic moduli obtained from these experiments can be compared with those from the FEM simulations, and hence can be further used to estimate the microporosity of individual MHS.

3.3. Validation of the FEM model

The purpose of this section is to validate the entire FEM simulations, including the accuracy of the finite element mesh size and the capability to simulate the effective mechanical response of individual MHS. In all validation simulations, the 3D MHS model (Fig. 3a) was meshed with massive hexahedra. Since the hexahedra size is directly related to the accuracy of simulation results, it is necessary to optimize the number of hexahedra to save the computing time based on the premise that the simulation accuracy is sufficient. A number of calculations were performed on the same MHS with the same boundary conditions and material properties. To analyze the convergence of the simulation results for the $D = 3$ mm MHS, the selected number of hexahedra decreased from 85,344 to 3459 quadratic elements (i.e., including 85,344, 53,016, 37,592, 20,992, 13,336, 5092, and 3459); For the $D = 2$ mm MHS, the number of hexahedra decreased from 37,594 to 1536 quadratic elements (i.e., including 37,594, 23,928, 13,826, 9192, 5816, 2400, and 1536). Furthermore, a porosity of $\phi = 0$ was applied to the two simulated MHS (i.e., $D = 2$ and 3 mm).

The nominal strain ϵ and stress σ were calculated by following Eqs. (1) and (2) respectively. The spent computing time was recorded and the first-collapse stress C can be obtained from the nominal stress-strain curves (Fig. 6a and b). To choose the optimal mesh size that balances the efficiency and accuracy in the FEM simulations, the first-collapse stress of the MHS for each mesh size is compared with the one obtained from the finest mesh size, C_{finest} . The relative difference between the two collapse stresses is defined as $(C - C_{\text{finest}})/C_{\text{finest}}$, and the results are summarized in Table 2. Both Fig. 6c and Table 1 show that the calculations converge to a constant value when the number of hexahedra has reached 53016 and 23,928 elements for the $D = 3$ and 2 mm MHS, respectively. Therefore, in subsequent simulations, a total of 53016 and 23,928 elements are eventually adopted for the $D = 3$ and 2 mm MHS, respectively.

3.4. FEM simulations of the compression of individual MHS with patterned porosity distributors

In this section, individual MHS FEM models with five differently patterned microporosity distributions were used to simulate the quasi-static compression and to probe the effects of different porosity distributions on the deformation and failure of individual MHS. While Table 1 summarizes all 10 different FEM models with different porosity

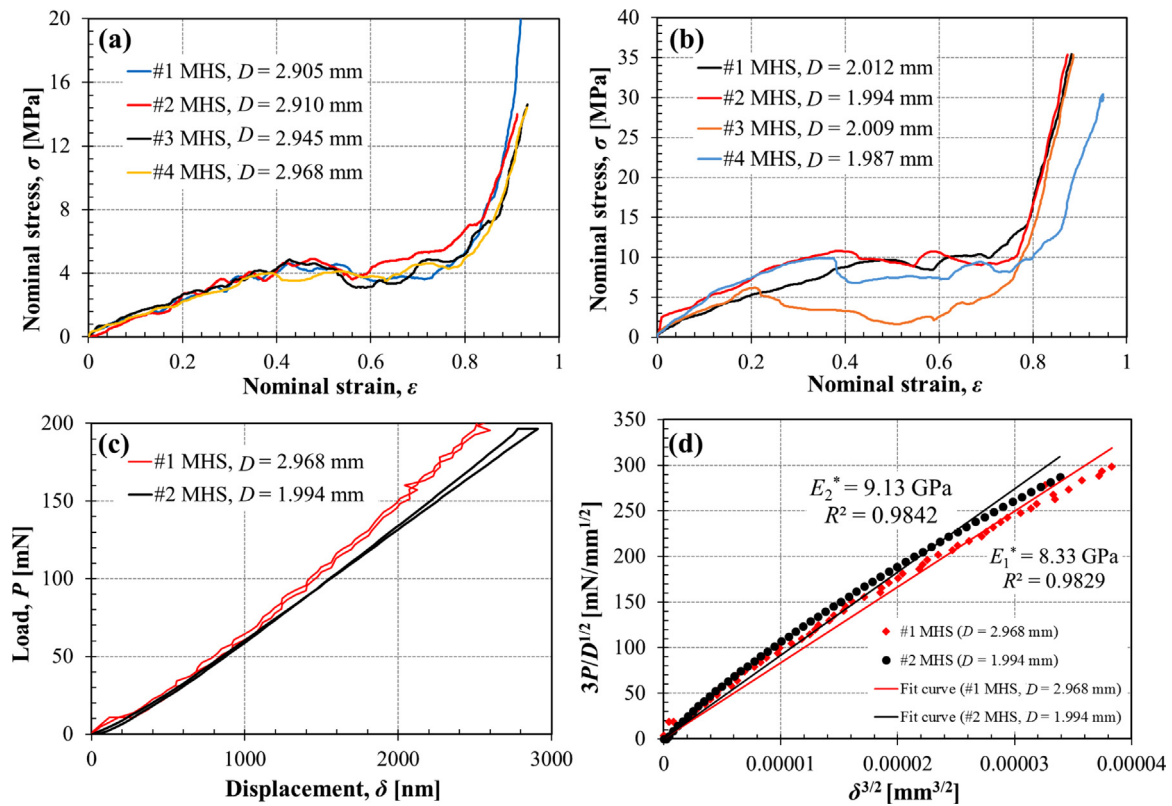


Fig. 4. Results of quasi-static compression testing and purely elastic compression testing: (a) and (b) nominal stress-strain compression curves for eight selected individual MHS with $D \approx 3$ and ~ 2 mm, respectively; (c) Experimental curves for two purely elastically compressed individual MHS ($D = 2.968$ and 1.994 mm); (d) Fitting of the purely elastic load-displacement curves with Hertz elastic contact theory.

distributions, D , t , and Φ , Fig. 7 compares the simulated results in terms of the nominal stress-strain curves. The simulated MHS compression behavior for each type of patterned porosity distribution is further discussed in detail in the following sections.

3.4.1. Behavior of MHS with uniform distribution of microporosity (UDM)

For the FEM model, UDM-MHS-1 (i.e., $D = 3$ mm, $t = 0.02$ mm, Table 1), a total of 8 different microporosities ranging from 0% to 32.88% (Fig. 7a), each with a uniform distribution, were simulated. While Fig. 7a compares the eight simulated nominal stress-strain

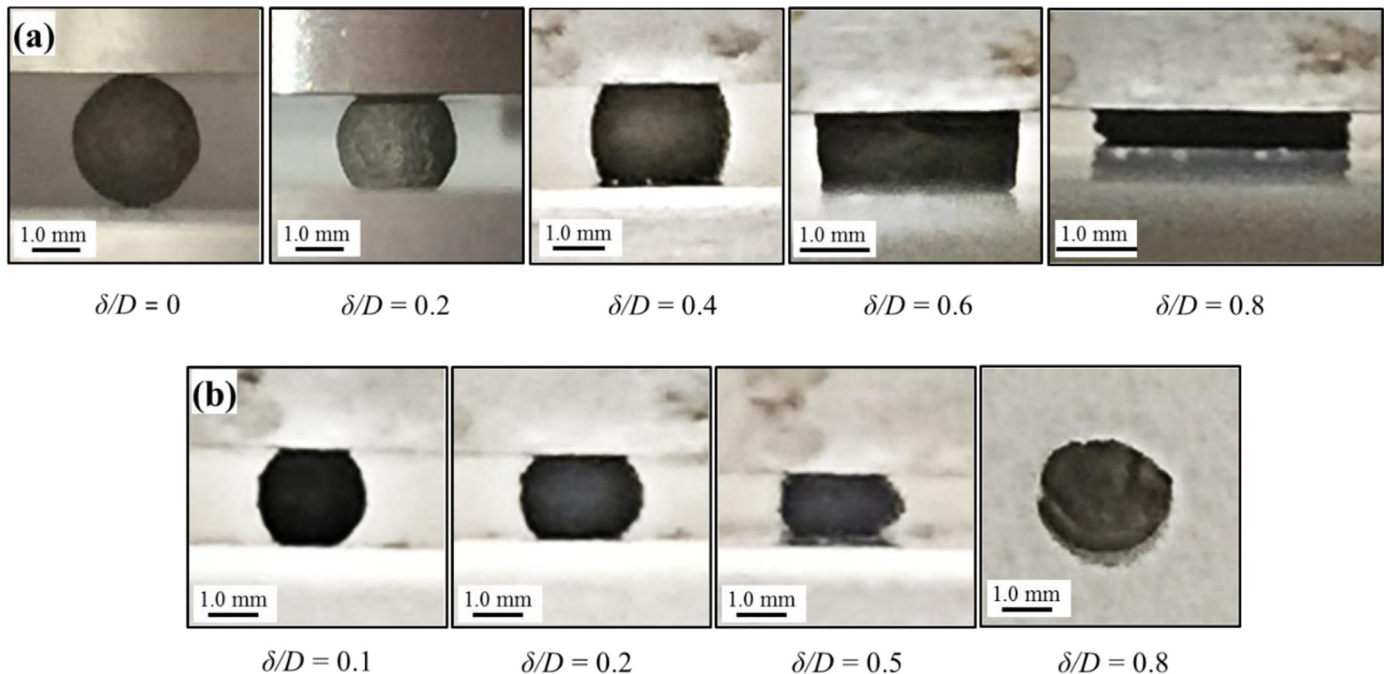


Fig. 5. Snapshots of the deformation process of a single MHS during quasi-static compression testing at a displacement rate of $\nu = 8 \times 10^{-7}$ m s⁻¹: (a) $D = 2.968$ mm; (b) $D = 1.994$ mm.

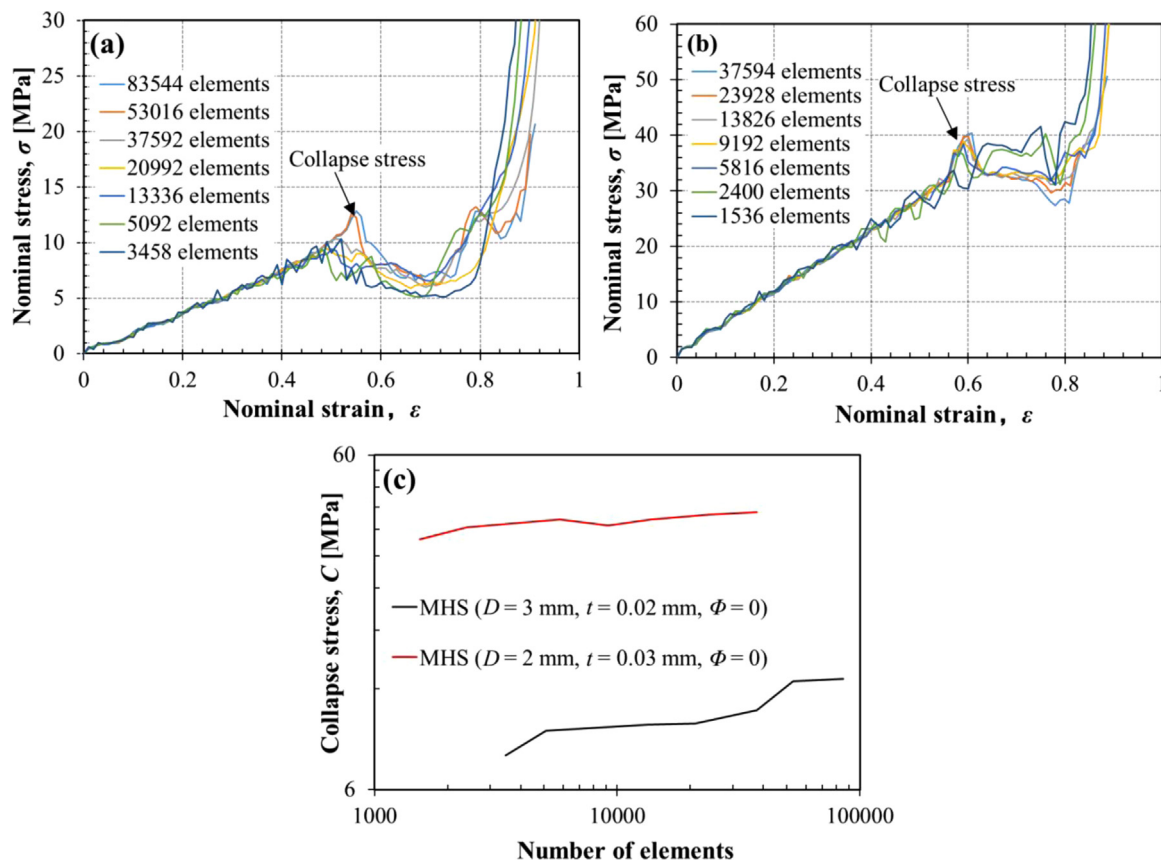


Fig. 6. Effects of FEM mesh size or the number of elements on the simulated stress-strain response of individual MHS: (a) and (b) nominal stress-strain curves of individual MHS with $D = 3$ and 2 mm respectively obtained by different mesh resolutions; (c) the relationship between the collapse stress and number of elements for the two simulated MHS.

curves, Fig. 8 highlights, with selected snapshots of the simulated deformation process for the MHS using $\phi = 0$ as an example, the von Mises stress evolution in the thin wall (where the blue colors represent the elastic zones, and the red ones represent the plastic (or yielded) zones) as well as the change in MHS geometry during compression. The entire compression process can be divided into the following five stages (Fig. 7a):

- Stage I ($\delta/D = 0-0.55$): elasto-plastic deformation. This stage is mainly characterized by the nearly linear nominal stress-strain curves but with many small serrations (Fig. 7a). It can be observed that, after a very small elastic deformation commencing immediately with the onset of compression, localized plastic deformation occurs near the wall-platen contacts, resulting in a wall-buckling failure at the center line (Fig. 8 at $\delta/D = 0.1$). As the compression continues, two indents develop on the top and bottom

contacts, and the contacts between the MHS and two platens transform from point to circular line contacts. Although the stresses at the two contact interfaces increase, the equator of the MHS remains a circular shape still with elastic deformation. These observations are consistent with previous work [17]. Moreover, the stress distribution at the contact perimeters are axisymmetric. That is, a linear work-hardening rate is applicable until the nominal strain reaches up to 0.55. It is noteworthy that the first self-contact of the MHS internal surface is suggested by several researchers to occur at $\delta/D = 0.5$ based on their dynamic and quasi-static compression testing [4,17]. However, this study demonstrates that such a phenomenon can actually occur before or after $\delta/D = 0.5$, which will be further discussed later.

- Stage II ($\delta/D = 0.55-0.7$): buckling and yielding of the upper wall. Buckling failure first occurs at the region of the side wall that is closer to the top platen at $\delta/D = 0.6$ (Fig. 8). Then further

Table 2

Effect of mesh resolution on the collapse stress and computing time of two MHS with different diameters and wall thicknesses.

MHS ($D = 3$ mm, $t = 0.02$ mm, $\phi = 0$)			MHS ($D = 2$ mm, $t = 0.03$ mm, $\phi = 0$)		
Number of elements	Collapse stress difference (%)	Computing time (h)	Number of elements	Collapse stress difference (%)	Computing time (h)
85,344	0	65.0	37,594	0	10.0
53,016	1.63	30.0	23,928	1.58	3.5
37,592	19.44	10.5	13,826	4.58	1.2
20,992	26.44	3.5	9192	8.46	1.0
13,336	26.91	1.0	5816	4.83	0.5
5092	30.02	0.5	2400	9.87	0.3
3459	40.90	0.2	1536	16.82	0.1

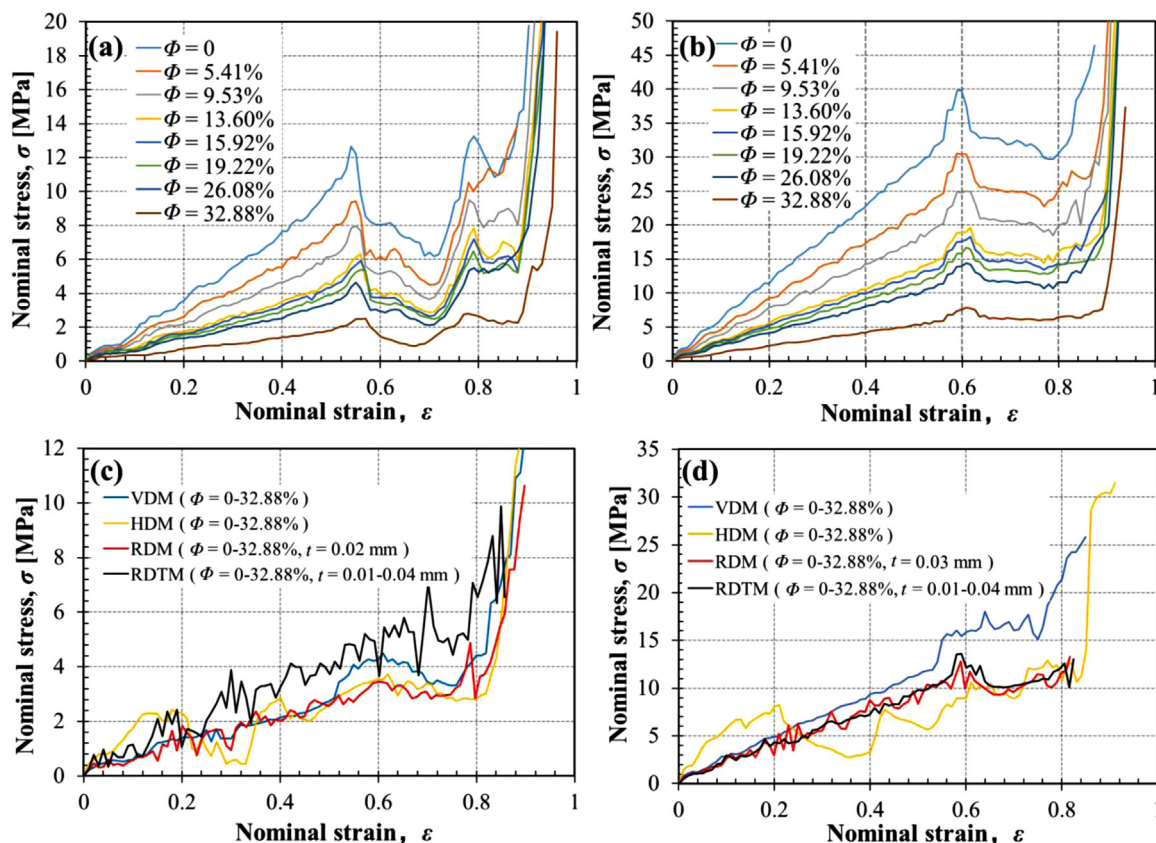


Fig. 7. Nominal stress-strain curves obtained by FEM simulations: (a) and (b) individual MHS of $D = 3$ and 2 mm respectively with different UDM ($\phi = 0$ – 32.88%); (c) and (d) individual MHS of $D = 3$ and 2 mm respectively with VDM, HDM, RDM and RDTM ($\phi = 0$ – 32.88%).

compression changes the circular line contact to a quadrangular line contact and thus the stress within the wall are redistributed. The buckling failure ends until $\delta/D = 0.7$, causing a remarkable drop in the nominal stress (Fig. 7a).

- Stage III ($\delta/D = 0.7$ – 0.8): transition stage. After the upper portion of the MHS wall collapses, the contact area between the MHS and top end platen increases, and a short densification process commences. Therefore, the stiffness of the MHS increases at this stage due to the occurring of more self-contacts of the MHS as well as the enhanced upper contacts.
- Stage IV ($\delta/D = 0.8$ – 0.84): buckling and yielding of the lower wall. New buckling failures occur at the lower wall after Stage III finishes. This stage is very similar to, but lasts much shorter than, Stage II.
- Stage V ($\delta/D > 0.84$): densification. Further compression is mainly dominated by the continuous increase in the number of self-contact points of the MHS as well as the number of MHS-end platen contact points after the majority of the wall collapses. The densification process continues to the end of compression, and the stiffness of the densified MHS increases significantly with further deformation.

However, the MHS with a smaller diameter ($D = 2$ mm, $t = 0.03$ mm, designated as UDM-MHS-2, Table 1) behaves differently during the compression process. This MHS only experiences four stages of compression deformation (Figs. 7b and 9). In Stage I ($\delta/D = 0$ – 0.55), the same compression behavior, but with a much higher nominal stress obviously owing to a higher t/D ratio, is observed when compared with the compression of the UDM-MHS-1. Stage II ($\delta/D = 0.55$ – 0.6) is the same as the one discussed above. In Stage III ($\delta/D = 0.6$ – 0.8), the buckling failure takes place at the equator rather than at the sphere-end platen contacting interfaces when $\delta/D = 0.6$. More importantly, deformation occurs synchronously at both the top and bottom contact interfaces, and hence the equator wall buckling is axisymmetric. In

Stage IV ($\delta/D > 0.8$), the MHS starts to become densified and this process lasts to the end of compression. In summary, these modeling results demonstrate that the t/D ratio can affect significantly the compression and failure behavior of individual MHS when the thin wall has a uniform distribution of microporosity and uniform wall thickness. These findings agree well with previous work concluding that a critical t/D ratio significantly affects the deformation mechanisms of the MHS thin wall after buckling occurs [17]. On the other hand, microporosity has little effect on the overall compression and failure behavior for the UDM-MHS with a certain t/D ratio, but it reduces the overall load-bearing capability (Fig. 7a and b). The relative collapse stress decreases with porosity, because the mechanical properties are weakened by the increase in microporosity. For instance, the modeling results show that the UDM-MHS-1 with a porosity $\phi = 32.88\%$ loses 80% of the load-bearing capability of the same sized MHS with zero microporosity. Therefore, microporosity is still of vital importance for the structural or functional applications of MHS as well as MHS-based materials, particularly for their load-bearing performances.

3.4.2. Behavior of MHS with vertical distribution of microporosity (VDM)

The compression behavior of a single VDM-MHS-1 ($D = 3$ mm, $t = 0.02$ mm, Table 1) with VDM is shown in Figs. 7c and 10. As the compression commences, both the top and bottom end platens are in contact with the wall with varied material properties (i.e., due to different porosities, Fig. 3b) at the same time. Compared with the UDM-MHS-1, the VDM-MHS-1 exhibits different deformation and failure behavior. First, during initial compression ($\delta/D < 0.5$), the shape of the two indents at the top and bottom contacting interfaces is irregular instead of a regularly-shaped circle. The reason is that, in the early compression, the wall sections with relatively higher porosities (e.g., 26.08% and 32.88% in this model) have smaller Young's moduli and yield strengths, and hence they can be regarded as weak regions within

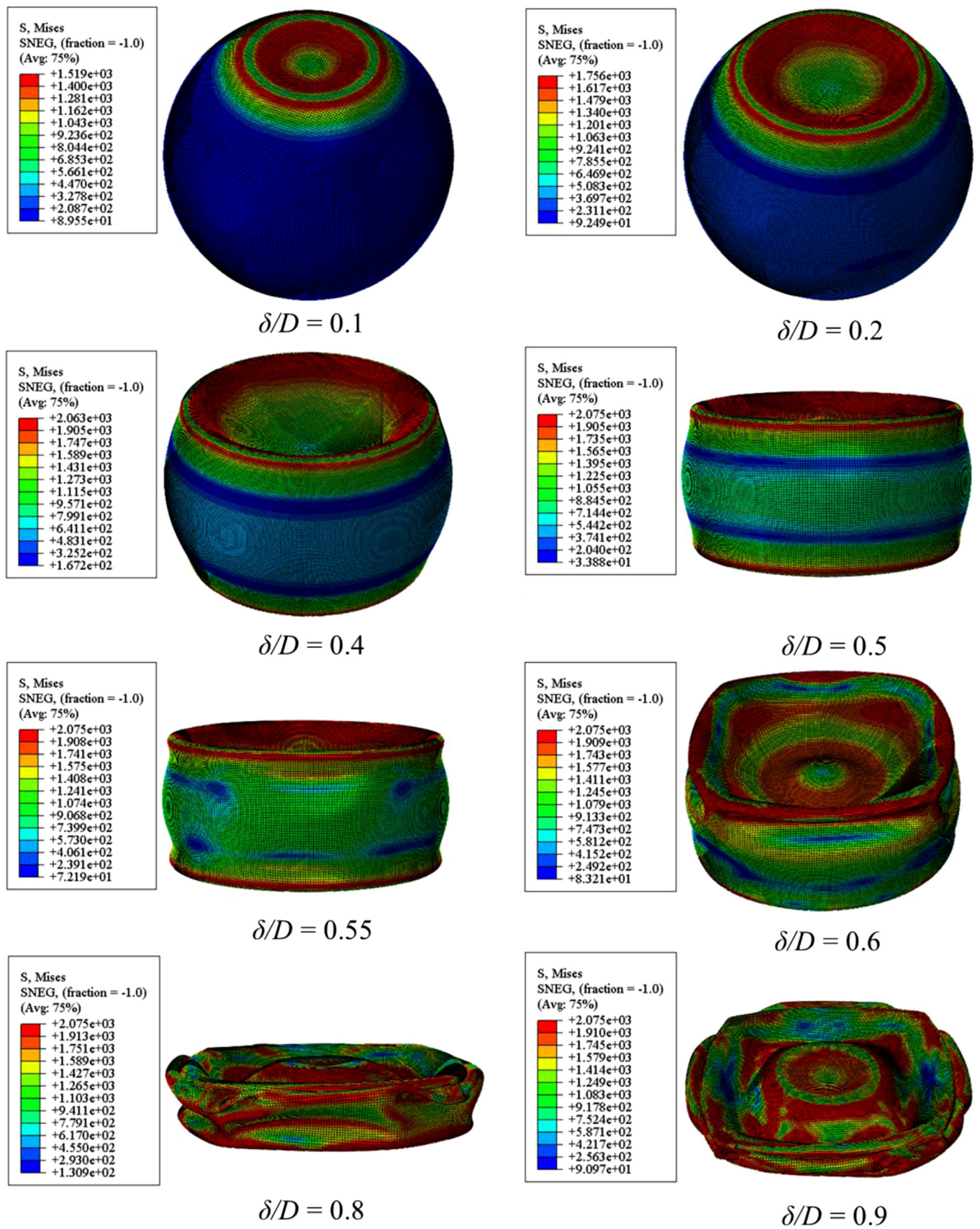


Fig. 8. Snapshots of simulated deformation process of a MHS with UDM ($D = 3 \text{ mm}$, $t = 0.02 \text{ mm}$, $\Phi = 0$) during quasi-static compression at $v = 8 \times 10^{-7} \text{ m s}^{-1}$ where the von Mises stress distributions are shown for each stage of deformation. (For interpretation of the references to color in this figure legend, the reader is referred to the web version of this article.)

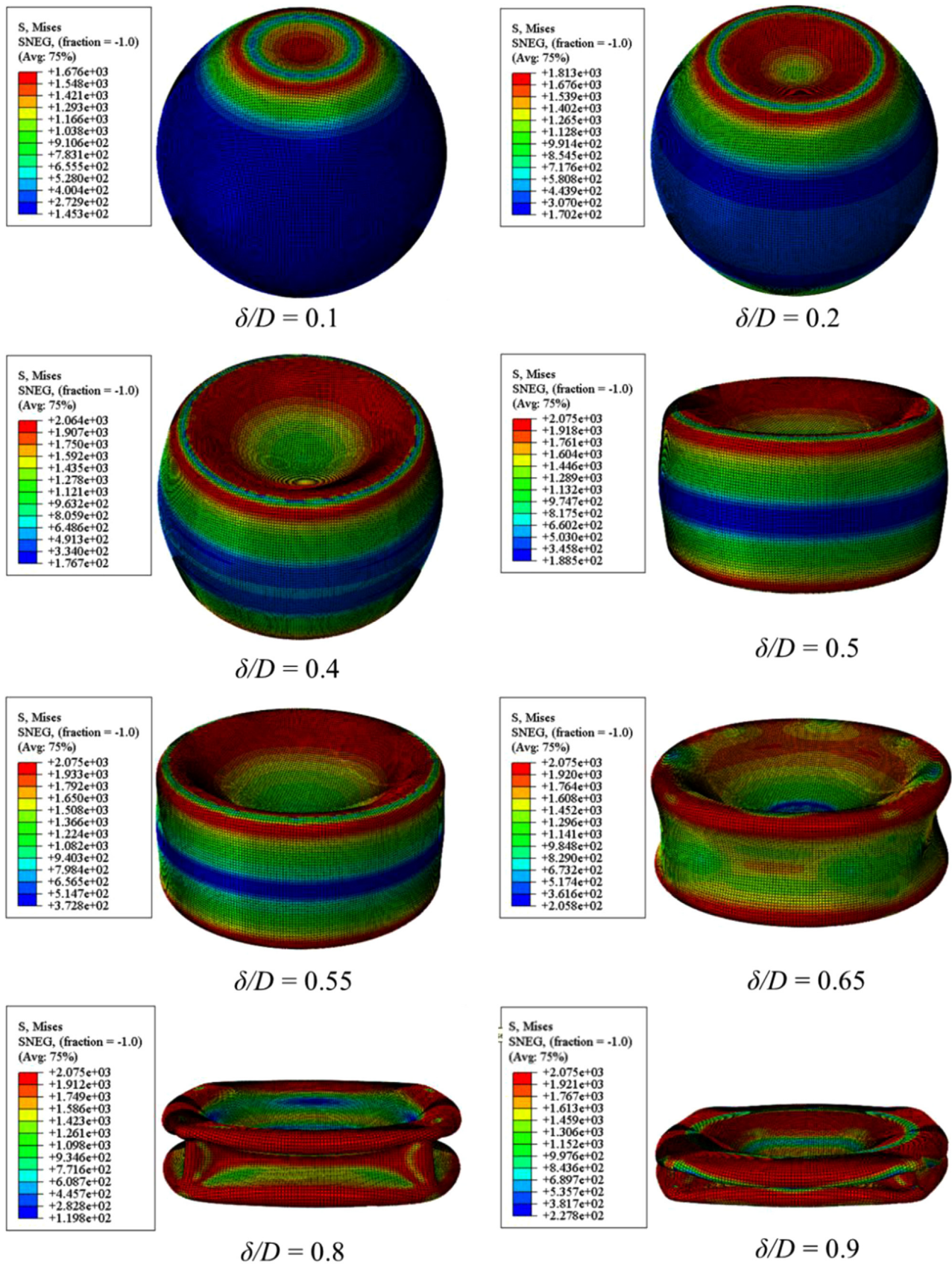


Fig. 9. Snapshots of simulated deformation process of a MHS with UDM ($D = 2$ mm, $t = 0.03$ mm, $\Phi = 0$) during quasi-static compression at $v = 8 \times 10^{-7}$ m s $^{-1}$ where the von Mises stress distributions are shown for each stage of deformation.

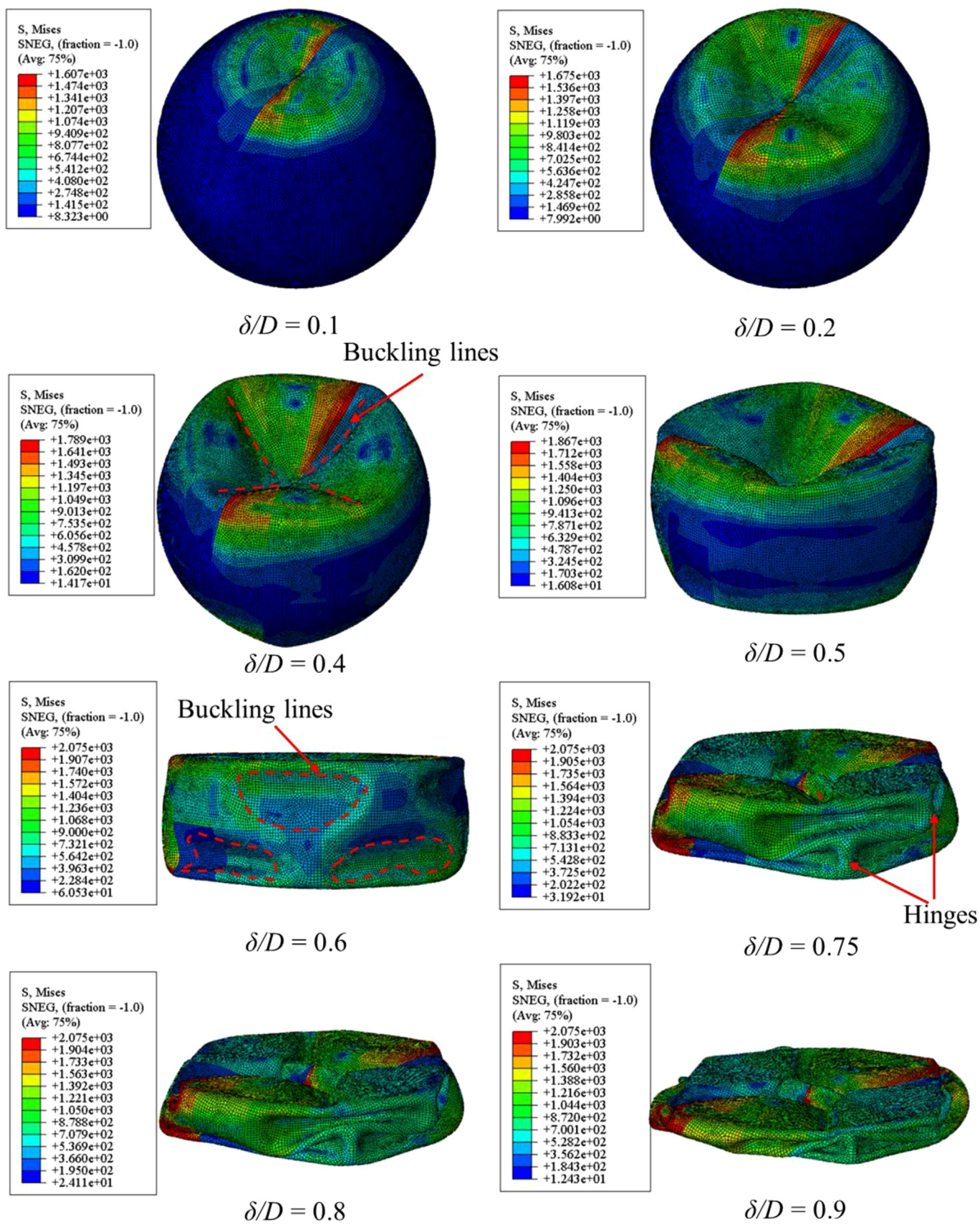


Fig. 10. Snapshots of simulated deformation process of a MHS with VDM ($D = 3$ mm, $t = 0.02$ mm, $\phi = 0-32.88\%$) during quasi-static compression at $v = 8 \times 10^{-7}$ m s⁻¹ where the von Mises stress distributions are shown for each stage of deformation.

the MHS wall. Fig. 7a and c show that the nominal stress in this MHS with mixed microporosities is higher than that of UDM-MHS-1 with a porosity of 26.08% or 32.88% when δ/D is < 0.25 . Upon further compression, the sections with higher microporosities (e.g., 32.88% and 26.08%) first undergo buckling failure, leading to a change in the wall-end platen contacting geometry. It is clearly seen that the weaker sections buckle first and buckling lines occur in the middle of the weaker sections, so there is a “line” in each weaker buckling segment. Furthermore, after $\delta/D = 0.5$, the first self-contact of the MHS internal surface occurs, and the nominal stress then increases, indicating that the first self-contact improves the load-bearing capability remarkably. At $\delta/D = 0.6$, buckling failures occur around both the MHS-top platen and MHS-bottom platen contacts, but not the equator. Since all buckling failures occur in the side wall under the “buckling line” of the two indents, it means that the weaker sections on a single MHS always first suffer from buckling failures during the entire compression process. After a large section of the wall collapses, the final densification stage appears. In general, if a relatively high microporosity exists in some sections of the MHS wall, it will affect the overall compression behavior as well as the load-bearing capability of individual MHS significantly.

For the single VDM-MHS-2 (i.e., $D = 2$ mm, $t = 0.03$ mm, Fig. 11), its compression behavior is similar to that of the UDM-MHS-2. Although the “buckling lines” existing within the two indents are obvious, overall buckling failure still occurs at the equator and under the “buckling lines” of the weaker sections. The nominal stress σ is higher than that of UDM-MHS-1 with a porosity of 26.08% and 32.88%, and this is perhaps caused by the higher t/D ratio. In general, when t/D is higher, the MHS is not so prone to buckling failure, and the overall buckling failure still occurs at the equator.

3.4.3. Behavior of MHS with horizontal distribution of microporosity (HDM)

The compression behavior of the HDM-MHS-2 ($D = 2$ mm, $t = 0.03$ mm, Table 1) is shown in Figs. 7d and 12. It can be seen that the HDM-MHS-2 exhibits the same deformation behavior as the UDM-MHS-2 when $\delta/D < 0.15$. However, at $\delta/D = 0.2$, the horizontal section with a porosity of 32.88% first deforms outward with significant lateral deformation, which is quite different from the behavior of other MHS described above. As the compression continues, the sections with other porosities experience buckling failures, typically starting successively from sections with relatively higher porosities to these with smaller ones (i.e., from 26.08% to 5.41%). In Fig. 7d, each mutational site represents one buckling section with a certain porosity. In the meanwhile, the top and bottom indents do not contact until the commencement of the densification process. In Fig. 5, the two experimental samples show a similar deformation process, and their experimental stress-strain curves show multiple zigzags or serrations (Fig. 4b). Because of the similar behavior, the “zigzag” phenomenon can be explained by the fact that several tested MHS contain imperfections in their thin walls, such as a large weak section of wall with a higher porosity or a thinner thickness, leading to the pre-matured buckling of the weakest regions, followed by the continuous buckling of other weaker regions. It can be inferred that the number of zigzags in the stress-strain curves indicates the number of weaker regions. It is worth pointing out that, in the experimental results, some weak regions in the MHS wall have poor ductility, and hence some fractures occur during compression. The simulated compression behavior of HDM-MHS-1 ($D = 3$ mm, $t = 0.02$ mm, Table 1) is nearly the same as that of the HDM-MHS-2, so it is not discussed here in detail.

3.4.4. Behavior of MHS with random distribution of microporosity (RDM) and random distribution of wall thickness and microporosity (RDTM)

As shown in Figs. 13 and 14, the compression process of RDM-MHS-1 and RDM-MHS-2 seems identical to that of UDM-MHS when $\delta/D < 0.5$. However, the indented surfaces of the RDM-MHS are not smooth, and the shape of the contact line is an irregular polygon instead

of either a circle or a regular polygon. With further compression, the randomly distributed weaker zones with higher porosities (e.g., $\Phi = 32.88\%$ or 26.08%) buckle first and become indented. Adjacent buckled zones are then linked, forming “buckling lines” on the MHS surface, as indicated by the dotted red lines in Figs. 13 and 14. In fact, subsequent buckling failure occurs along these “buckling lines”. In contrast, those relatively stronger regions (i.e., sections with a lower porosity) transform into some hinges that fail during the final stage of densification and make contributions to the increased load-bearing capability before the MHS eventually becomes a thinly compressed sheet.

For the RDTM-MHS, it can be observed that the compression process of the RDTM-MHS is similar to that of the RDM-MHS, but the failure process is different (Figs. 15 and 16). The two controlling factors for buckling failure are porosity and wall thickness, and thus the sections possessing combinations of a higher porosity and a thinner wall thickness are more prone to buckling. For example, the section with $\Phi = 32.88\%$ and $t = 0.01$ mm is most prone to buckling, and the one with $\Phi = 0$ and $t = 0.04$ mm is least prone to buckling. On the other hand, the porosity and wall thickness have mutual and coupled influences, and the “buckling lines” similarly occur at those adjacent sections with the weakest combinations of porosity and wall thickness. Therefore, the RDTM-MHS has the highest degrees of random properties and is the most complex case than any other aforementioned cases.

Although prior effort was made to characterize quantitatively the microstructure and microporosity of MHS thin walls [19], it requires some specialized facilities (e.g., XCT, SEM) and is time-consuming (e.g., image-processing). Even with the XCT or SEM techniques, only can a small section of the MHS be studied. The integrated experimental and computational study presented herein can help us assess quickly but qualitatively the overall porosity and wall thickness distributions for some manufactured MHS. For instance, comparison between the experimental and simulated nominal stress-strain curves (Figs. 4 and 7) can help understand roughly the variations of the porosity and wall thickness distributions. In fact, the compression behavior of the RDTM-MHS is likely the most presentative of the actual manufactured MHS. However, a few curves shown in Fig. 4b indicate that the MHS with $D = \sim 2$ mm and $t = \sim 0.03$ mm have a higher degree of variability in both porosity and thickness distributions, and some even contain a relatively large weaker sections such that it behaves similarly to the HDM-MHS models (e.g., HDM curves in Fig. 7c and d vs. #3 and #4 MHS curves in Fig. 4b). On the other hand, the MHS with $D = \sim 3$ mm and $t = \sim 0.02$ mm have smaller variability in porosity and thickness distributions.

3.4.5. Self-contacts of individual MHS with different microporosity distribution patterns

Some prior work concluded that the first self-contact of internal surface of a hollow sphere occurs at $\delta/D = 0.5$ under the quasi-static or dynamic compression [4,17]. However, based on the results discussed above, the first self-contact can actually take place either before or after the defined critical compression at $\delta/D = 0.5$. Figs. 17 and 18 show the deformed geometry of individual MHS with $D = 3.0$ and 2.0 mm respectively as well as varying porosity distribution patterns and wall thicknesses at $\delta/D = 0.5$, where one can find that the first self-contact occurs at $\delta/D > 0.5$ for most cases. For the HDM-MHS-1, the first self-contact begins at $\delta/D < 0.5$ due to the early buckling failure occurring at a large horizontal weak section with a high porosity ($\Phi = 32.88\%$). It should be noted that the VDM-MHS does not exhibit the same phenomenon because other strong sections surrounding the weak zones take most of the applied load. These observations suggest that the orientation of porosity distribution relative to the loading direction and the location and distribution of weak zones both have significant effects on the occurrence of first self-contact within the MHS. Besides, other MHS with different porosity distribution patterns and varied wall thicknesses can have the first self-contacts at $\delta/D > 0.5$. For example,

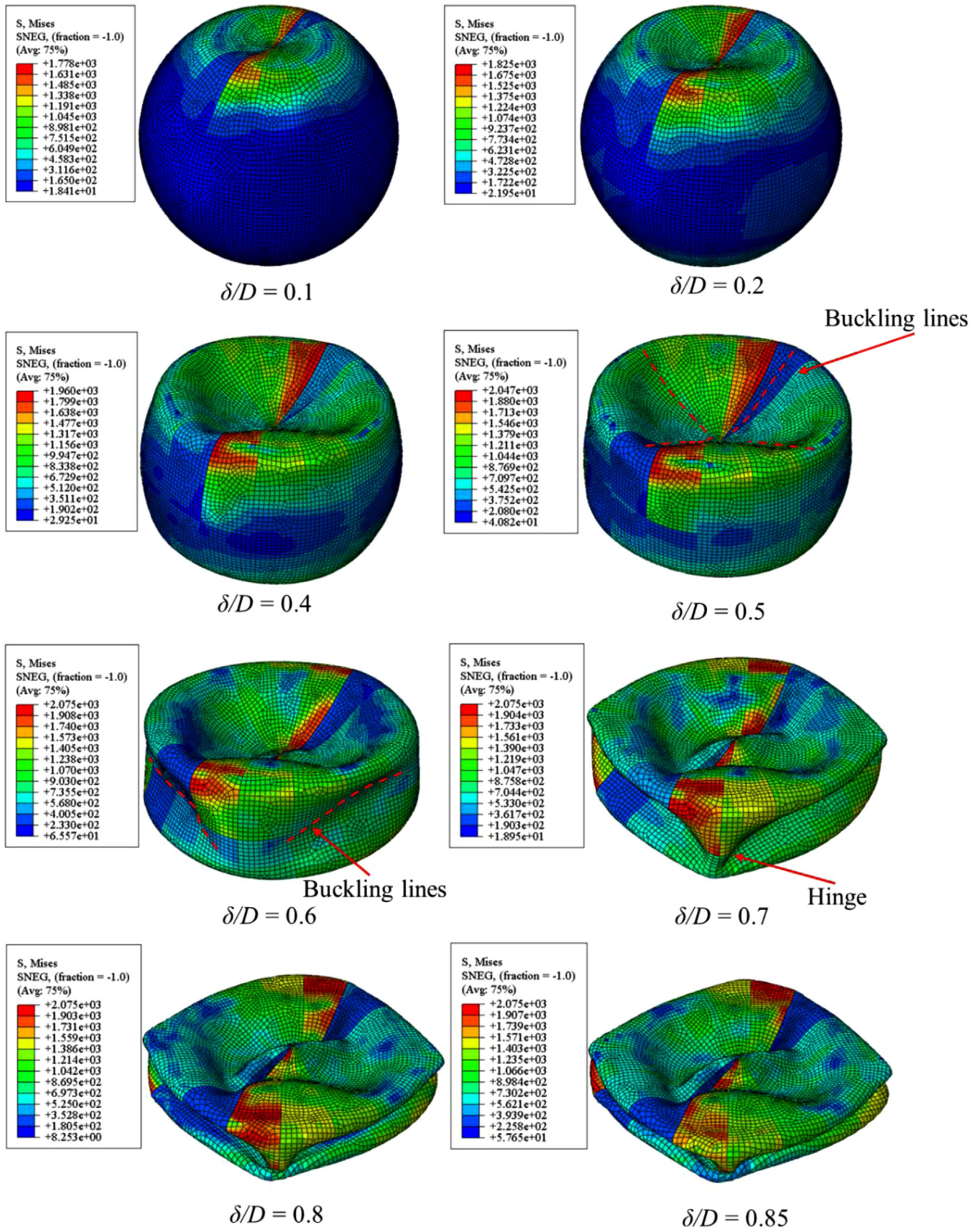


Fig. 11. Snapshots of simulated deformation process of a MHS with VDM ($D = 2 \text{ mm}$, $t = 0.03 \text{ mm}$, $\phi = 0\text{--}32.88\%$) during quasi-static compression at $v = 8 \times 10^{-7} \text{ m s}^{-1}$ where the von Mises stress distributions are shown for each stage of deformation.

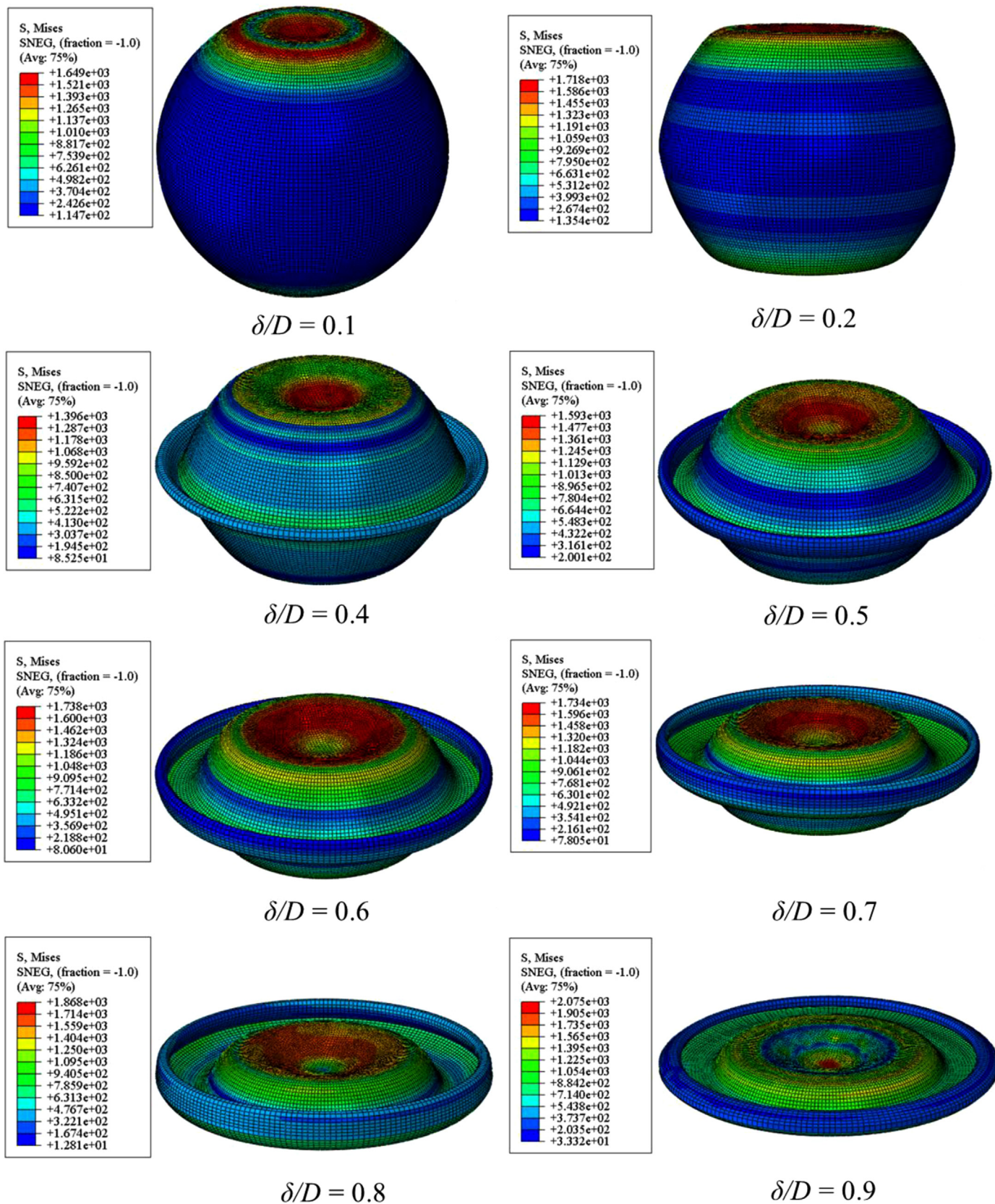


Fig. 12. Snapshots of simulated deformation process of a MHS with HDM ($D = 2$ mm, $t = 0.03$ mm, $\Phi = 0\text{--}32.88\%$) during quasi-static compression at $v = 8 \times 10^{-7}$ m s⁻¹ where the von Mises stress distributions are shown for each stage of deformation.

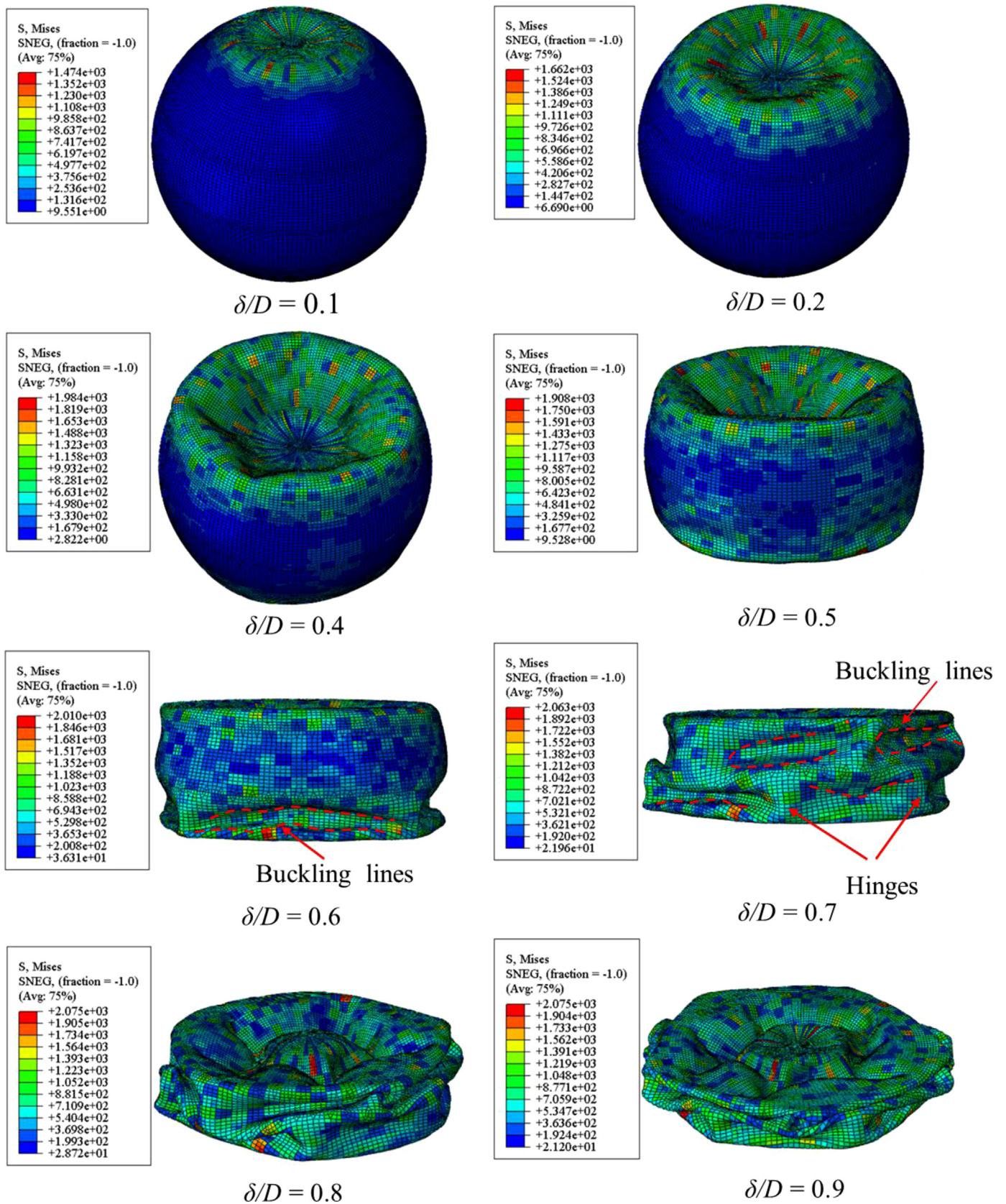


Fig. 13. Snapshots of simulated deformation process of a MHS with RDM ($D = 3$ mm, $t = 0.02$ mm, $\phi = 0-32.88\%$) during quasi-static compression at $v = 8 \times 10^{-7}$ m s⁻¹ where the von Mises stress distributions are shown for each stage of deformation.

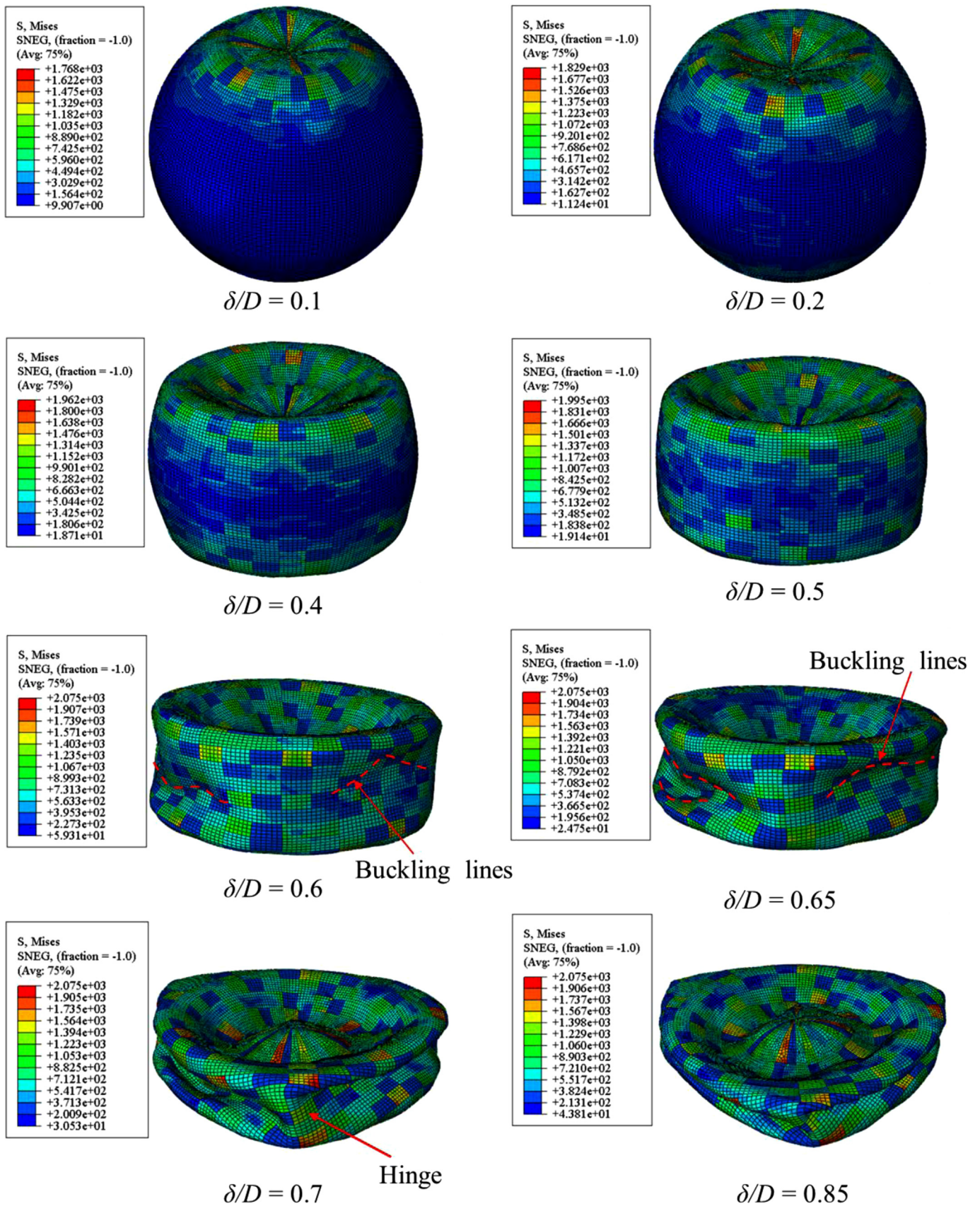


Fig. 14. Snapshots of simulated deformation process of a MHS with RDM ($D = 2$ mm, $t = 0.03$ mm, $\phi = 0-32.88\%$) during quasi-static compression at $v = 8 \times 10^{-7}$ m s⁻¹ where the von Mises stress distributions are shown for each stage of deformation.

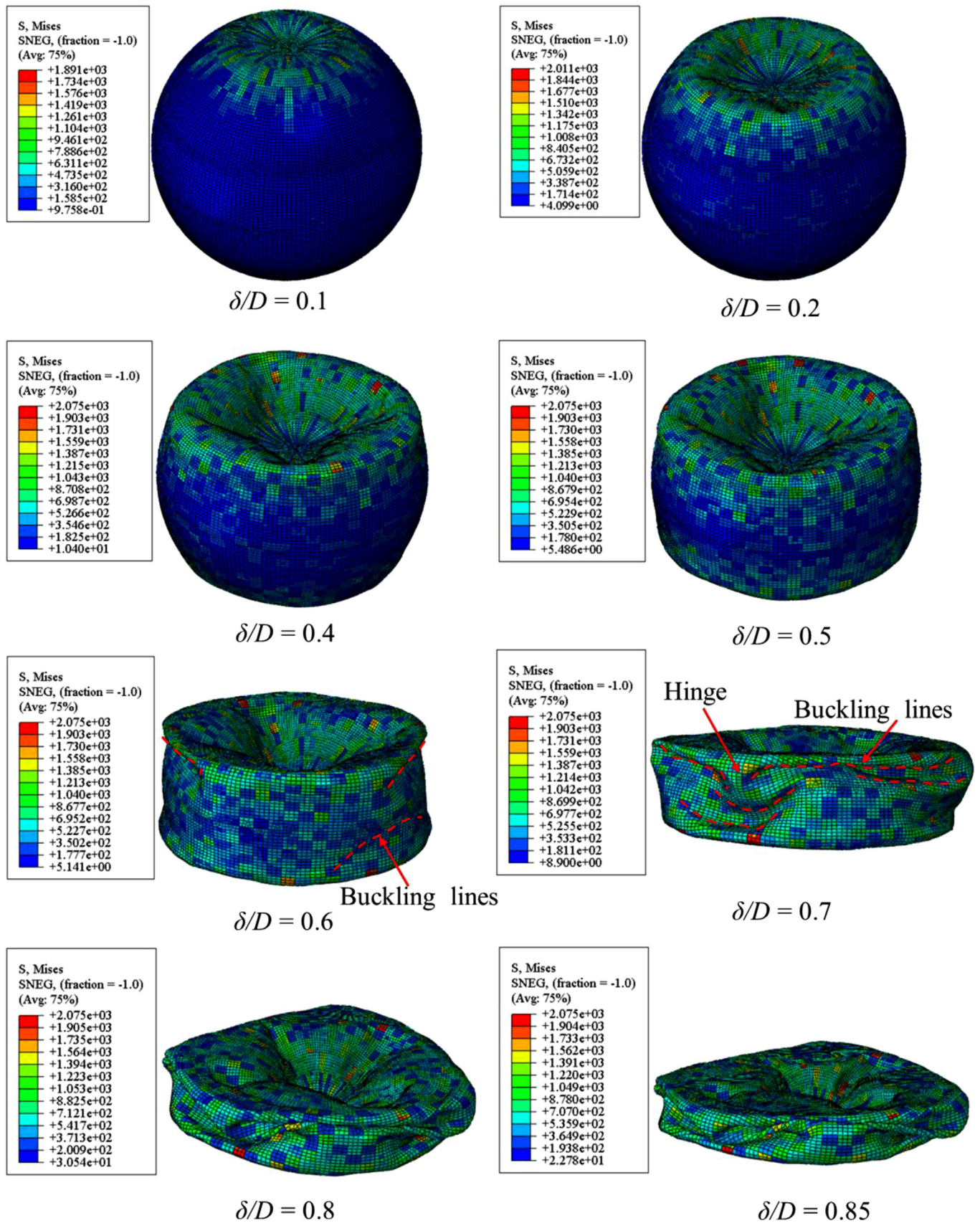


Fig. 15. Snapshots of simulated deformation process of a MHS with RDTM ($D = 3$ mm, $t = 0.01\text{--}0.04$ mm, $\phi = 0\text{--}32.88\%$) during quasi-static compression at $v = 8 \times 10^{-7}$ m s $^{-1}$ where the von Mises stress distributions are shown for each stage of deformation.

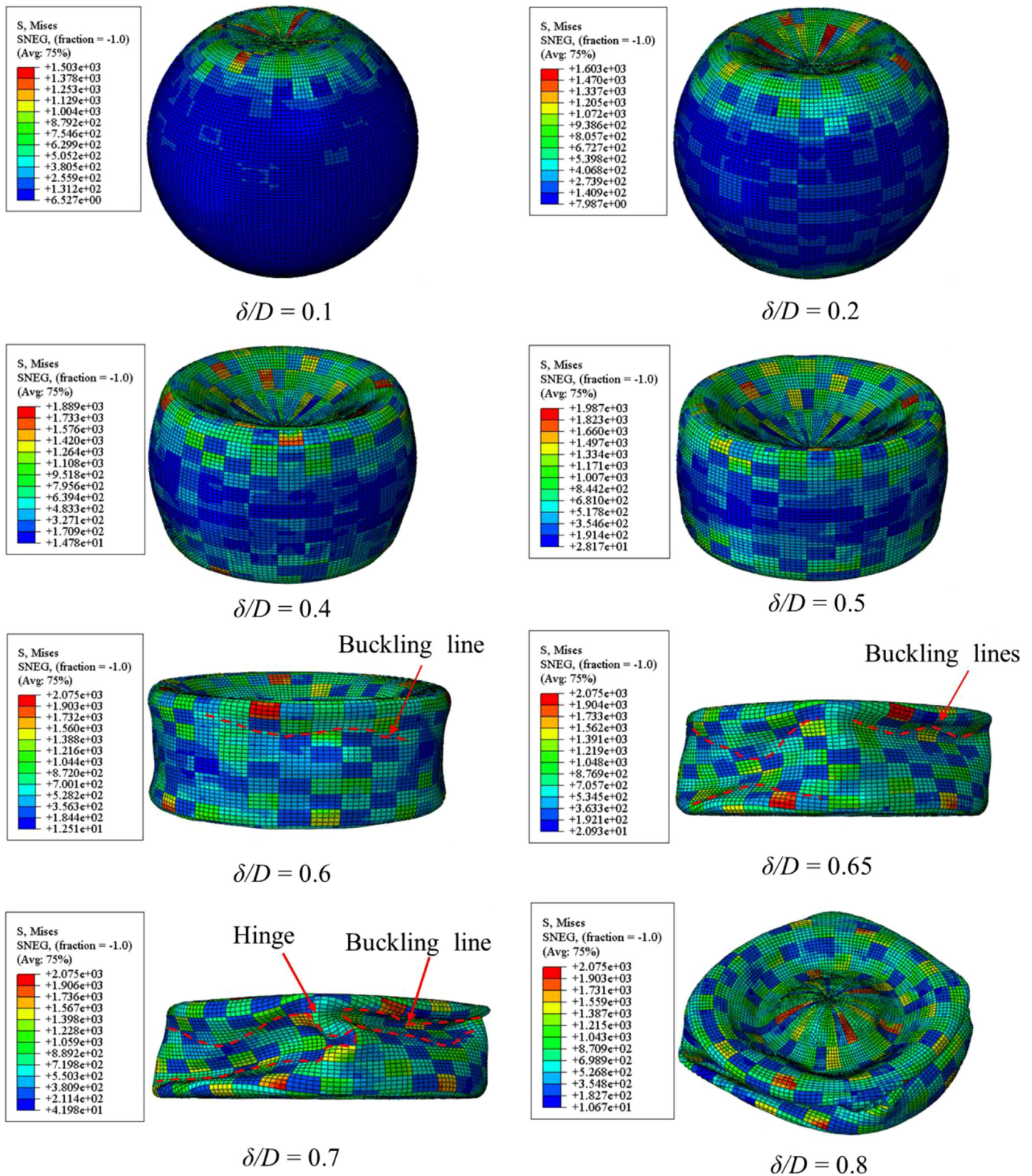


Fig. 16. Snapshots of simulated deformation process of a MHS with RDTM ($D = 2$ mm, $t = 0.01\text{--}0.04$ mm, $\phi = 0\text{--}32.88\%$) during quasi-static compression at $v = 8 \times 10^{-7}$ m s $^{-1}$ where the von Mises stress distributions are shown for each stage of deformation.

the first self-contacts of the RDM-MHS and RDTM-MHS with $D = 3$ and 2 mm all occur at $\delta/D > 0.5$.

3.5. Effect of porosity distribution patterns on elasticity and collapse stress of individual MHS

To evaluate the effects of different porosities on the elastic and collapse behavior of individual porous MHS, the eight UDM-MHS-2

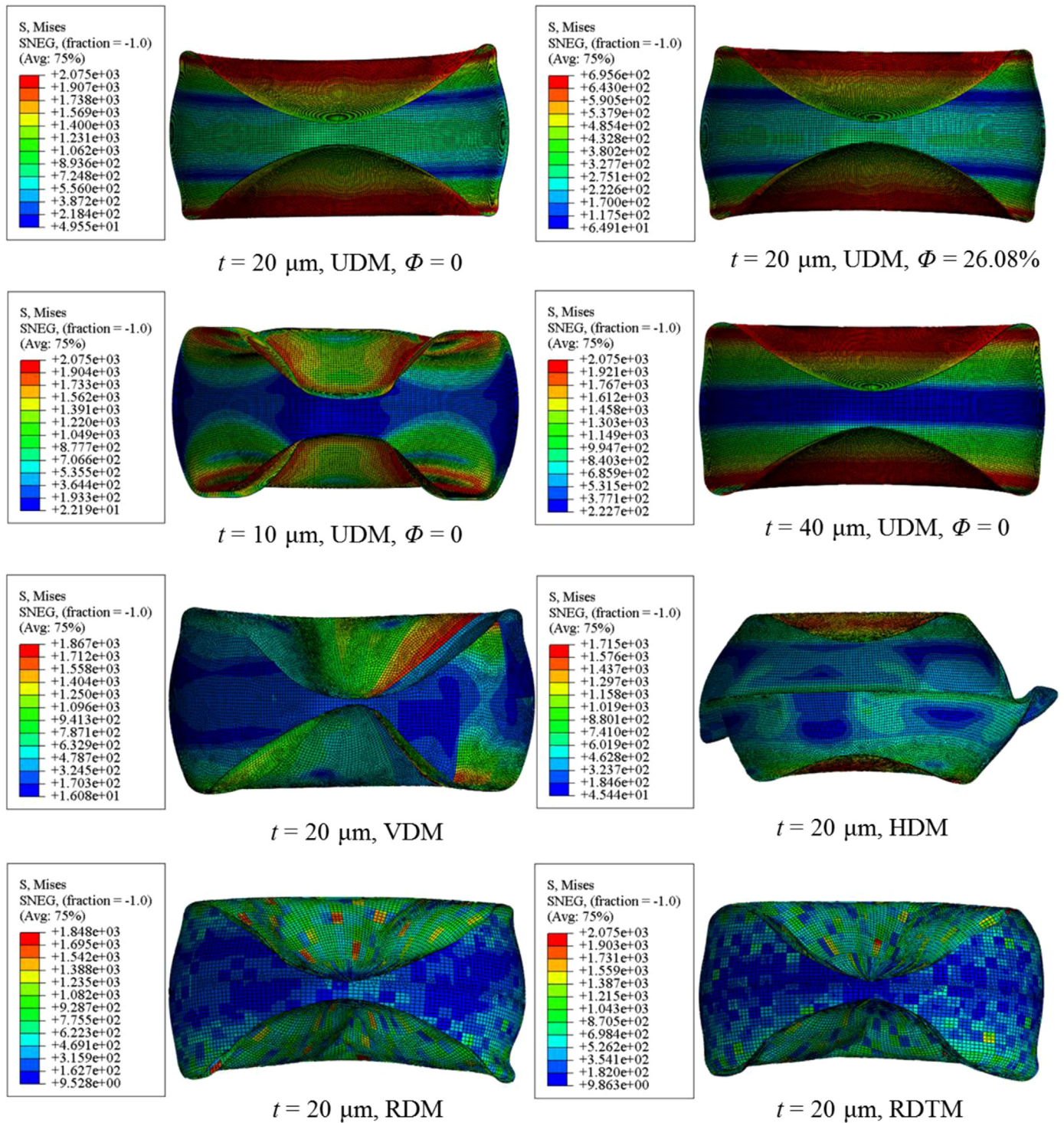


Fig. 17. Deformed geometry of individual MHS ($D = 3$ mm) with different porosity distribution patterns and thickness at $\delta/D = 0.5$.

FEM models (Table 1) are chosen as examples with the wall porosities ranging from 0% to 32.88%. In these simulations, the mechanical properties of the MHS thin wall are assumed to be the same as the local porous MHS thin wall in Song et al. [19]. For consistency with the purely elastic compression testing, a displacement-controlled method is adopted in these simulations and the maximum displacement is set to 2000 nm, almost the same as the one used in the purely elastic compression experiments.

Fig. 19a shows the simulated purely elastic loading-unloading curves of eight individual UDM-MHS-2 models with different porosities.

For comparison, the two experimental curves obtained from the purely elastic compression of two MHS (Fig. 4c) are also included in this figure. It can be seen that the loading segments overlap with the unloading segments for both the FEM simulations and experimental data under the controlled displacement of < 2000 nm. Therefore, both the eight UDM-MHS-2 FEM models and two experimentally tested MHS experience purely elastic compression and recovery. Fig. 19b shows the reduced moduli of the eight MHS with different porosities obtained from the simulation results obtained by using Hertz elastic contact theory. Obviously, with the thin wall porosity increasing, the reduced

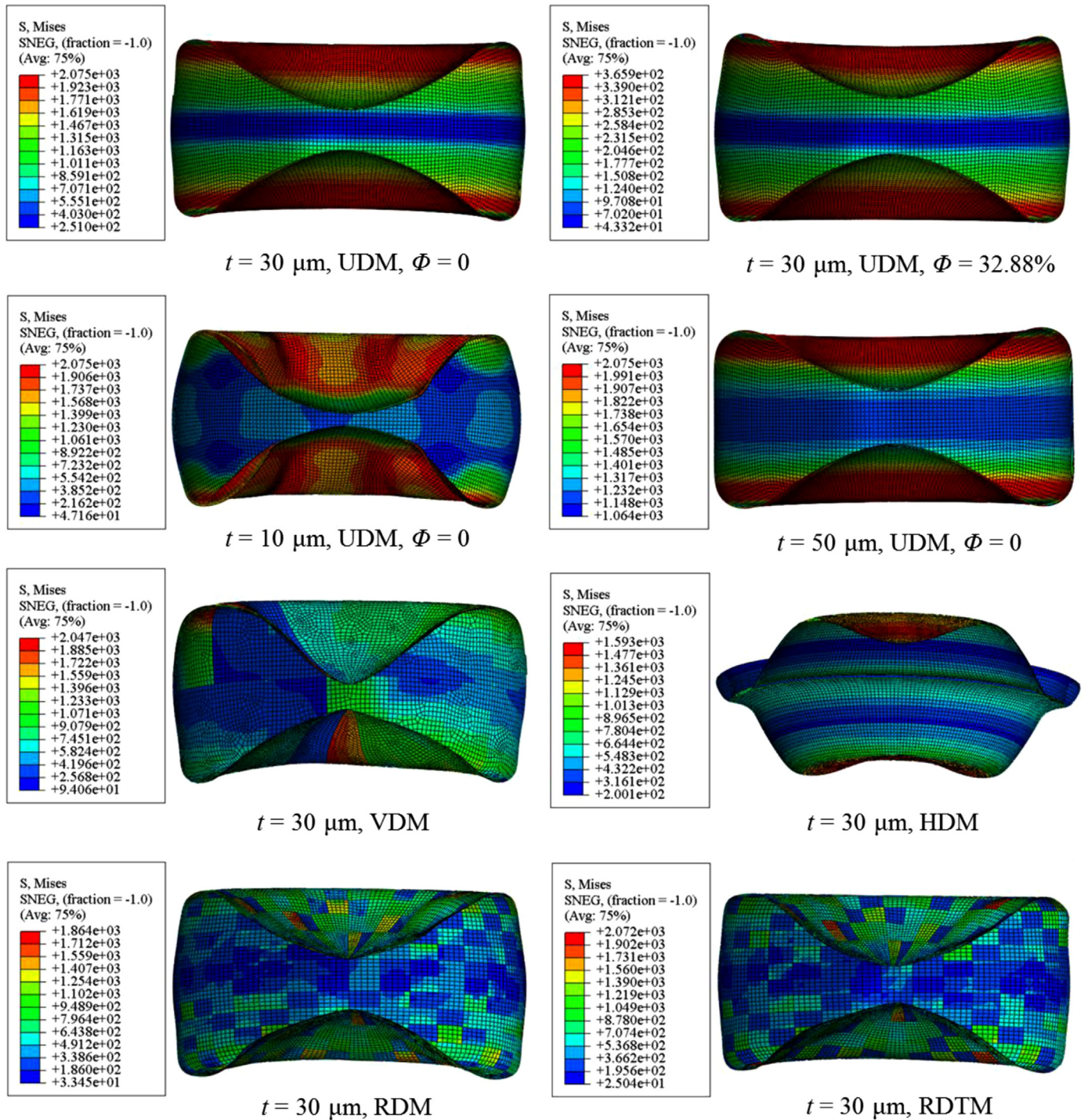


Fig. 18. Deformed geometry of individual MHS ($D = 2$ mm) with different porosity distribution patterns and thickness at $\delta/D = 0.5$.

modulus E^* decreases. To probe the relationship between the wall material's properties and the mechanical response of a whole MHS (i.e., the MHS as a thin-shelled structure), the FEM simulation results are also summarized in Table 3 and re-plotted in Fig. 19c. The Young's moduli of individual MHS decrease nonlinearly with increasing porosity, and these values can be fitted by the following equation:

$$\frac{E}{E_s} = \left(1 - \frac{\Phi}{0.847}\right)^{2.31} \quad (10)$$

where E and E_s are the Young's modulus of individual MHS with porous and non-porous thin wall, respectively; the coefficient of determination (i.e., R^2) for the fit equation is 0.9734. In fact, this equation is the same

as the one used to describe the dependence of the Young's modulus on microporosity for the porous MHS wall material studied in Song et al. [19], indicating that the Young's modulus of the porous wall also dominates the elastic behavior of individual MHS.

In addition to elastic behavior, the microporosity also plays an important role in the collapse of individual MHS. The collapse stress of each MHS with different porosities is extracted from Fig. 7b. By comparing the combined data in Table 3 and Figs. 7b and 19c, it is noted that the collapse stress of individual MHS is affected by the initial yield strength of the thin wall, and the collapse stress of MHS can be described by the same power-law function developed for the yielding of the porous MHS wall material [19]:

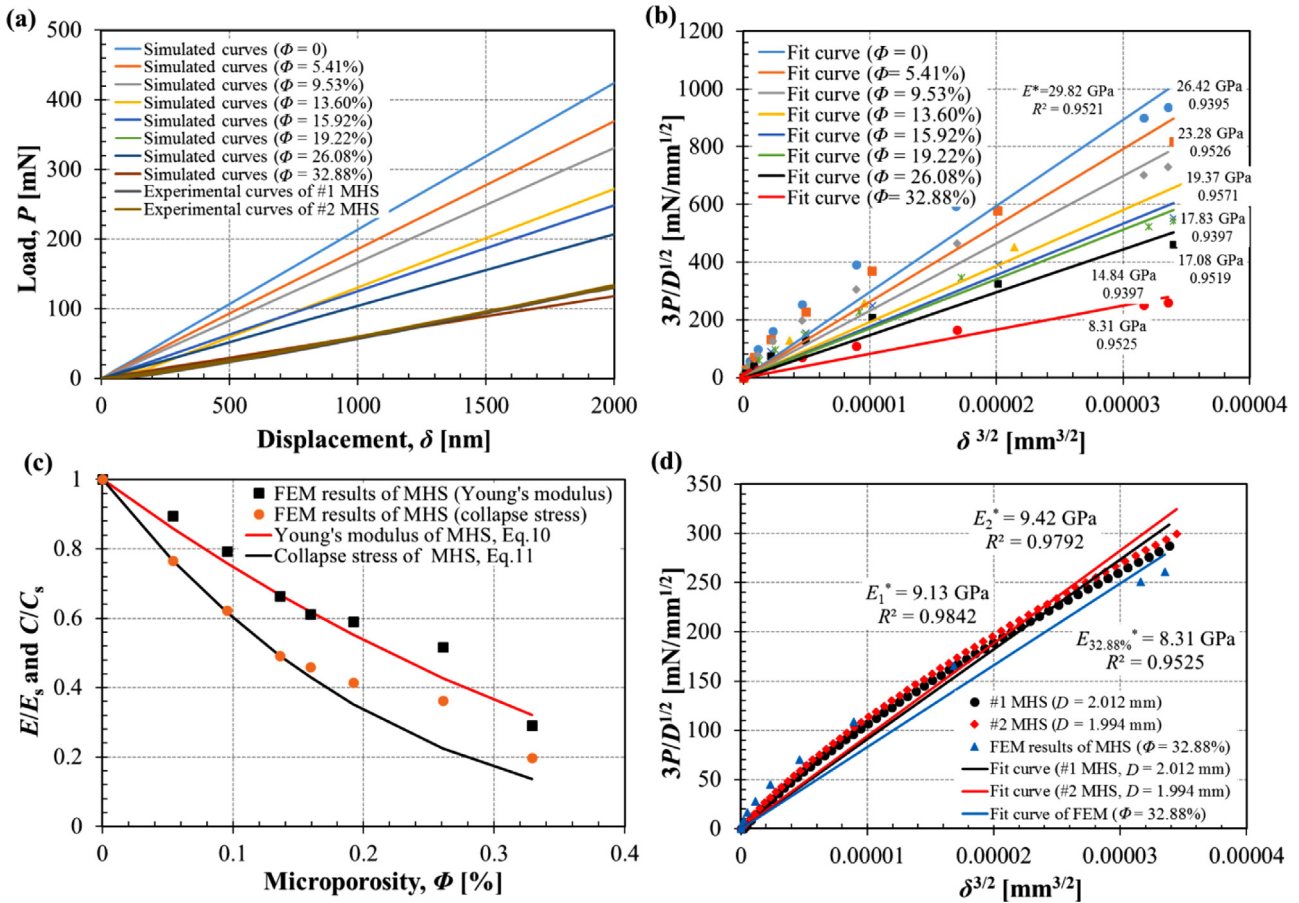


Fig. 19. (a) Simulated loading and unloading load-displacement curves of single UDM-MHS ($D = 2$ mm) with different porosities, compared with two experimental curves ($D = 2.012$ mm and 1.994 mm under purely elastic compression); (b) Fitting of the load-displacement curves with Hertz elastic contact theory; (c) Dependence of Young's modulus and collapse stress on microporosity, including FEM simulated results and fitted curves. (d) Fitting of the experimental curves of MHS ($D = 2.012$ and 1.994 mm) and the simulated curves for UDM-MHS ($D = 2$ mm, $\Phi = 32.88\%$) under purely elastic compression.

Table 3

Effect of microporosity on the Young's modulus and collapse stress of individual MHS with different but uniformly distributed porosity.

Sample ID	Φ (%)	E/E_s	C/C_s
1	0.00	1.00	1.00
2	5.41	0.90	0.77
3	9.53	0.79	0.62
4	13.60	0.66	0.49
5	15.92	0.61	0.46
6	19.22	0.59	0.41
7	26.08	0.52	0.36
8	32.88	0.29	0.20

$$\frac{C}{C_s} = \left(1 - \frac{\Phi}{0.847}\right)^{4.051} \quad (11)$$

where C and C_s are the collapse stress of individual MHS with porous and non-porous thin wall, respectively; the microporosity Φ in the range of $0 \leq \Phi \leq 50\%$ is considered in this study; the coefficient of determination (i.e., R^2) for this fit equation is 0.9830.

In general, the microporosity directly affects both the elastic and plastic behavior of individual MHS, and all of above results are consistent with the relationships linking the Young's modulus and yield strength with the thin wall microporosity. Therefore, during manufacturing, the microporosity should be well controlled as much as possible to tailor the desired mechanical properties of individual MHS and MHS-based foam materials.

Finally, the simulation results can also be used to quantitatively

estimate the porosity of manufactured MHS based on either the measured Young's modulus or collapse stress. Here is given a simple example. Fig. 19d compares the fit curves of two experimental compression curves and FEM simulation results for a UDM-MHS with a microporosity of 32.88%. Apparently, the thin wall microporosity of the two tested MHS is slightly smaller than 32.88% if the wall thickness is uniform, assumed to be 0.03 mm. In fact, it can be seen that there is little difference between the experimental and simulated results. This is attributed to the fact that, for the real manufactured MHS, the wall thickness is not uniform and microporosity is not homogeneously distributed. Instead, both the wall thickness and microporosity distribute randomly for the real manufactured MHS. In addition, the manufactured MHS also possess geometry imperfections, and are not a perfectly round hollow sphere as assumed in the FEM simulations. Nevertheless, this real manufactured MHS can still be simulated by the FEM MHS models with a wall thickness of 0.03 mm and a uniformly distributed porosity that is slightly lower than 32.88% (e.g., 30% or 31%). With Eq. (10), one can estimate the microporosity of the two tested MHS as $\sim 33\text{--}34\%$.

Based on the above discussion, it is logical to conclude that the foam materials manufactured based on this kind of MHS can be studied and modeled using the aforementioned individual MHS models and pertinent mechanical properties. The results from this study can be exploited to model the real MHS-based materials as well as the design and manufacturing of porous MHS.

4. Conclusions

This paper presents an integrated experimental and computational study to understand the effects of microporosity distribution in the thin wall on the overall deformation and failure behavior of MHS under quasi-static compression. Based on the above results and analyses, important conclusions can be drawn as follows:

- The entire deformation process of individual MHS with microporous thin wall under quasi-static compression can be subdivided into three different stages: buckling and yielding, collapse, and self-densification, and the failure is dominated by the buckling of its porous thin wall. The Young's moduli of two individual MHS with diameters of 2.968 and 1.994 mm are 7.64 and 8.37 GPa, respectively, obtained by purely elastic compression testing.
- The pattern of microporosity distributions within the thin wall significantly affects the deformation and failure behavior of individual MHS. The weak regions that have relatively high porosity and/or relatively small wall thickness buckle first, followed by sinking inwards, and those adjacent weak regions then form the “buckling lines” indicating the locations of buckling failure during the quasi-static compression, which is accompanied by generating hinges that contribute to the increased load-bearing capability toward the final densification stage.
- Depending upon the patterns of microporosity distribution in the thin wall, the self-contact of a single MHS during quasi-static compression can take place at either smaller or greater than the previously observed or defined boundary $\delta/D = 0.5$.
- The Young's modulus and collapse stress of the individual UDM-MHS are consistent with the Young's modulus and yield strength of the porous MHS thin wall, both of which decrease nonlinearly with increasing microporosity, and this relationship can be described by two power-law functions similar to those developed for the porous thin wall.

Acknowledgments

The first author (J.S.) was supported by a Visiting Scholarship awarded by the China Scholarship Council, China. This work was also partially supported by the corresponding author's startup fund provided by the Department of Civil and Environmental Engineering at the University of Massachusetts Amherst, including the acquisition of a Keysight G200 nanoindenter.

Data availability

The raw data and the processed data required to reproduce these findings are available from the first author or corresponding author (email: zhangg@umass.edu). Only limited raw/processed data required to reproduce these findings cannot be shared at this time as the data also forms part of an ongoing study.

References

[1] A. Rabiei, L.J. Vendra, A comparison of composite metal foam's properties and other comparable metal foams, *Mater. Lett.* 63 (2009) 533–536, <https://doi.org/10.1016/j.matlet.2008.11.002>.

[2] C. Park, S. Nutt, PM synthesis and properties of steel foams, *Mater. Sci. Eng. A* 288 (2000) 111–118, [https://doi.org/10.1016/S0921-5093\(00\)00761-9](https://doi.org/10.1016/S0921-5093(00)00761-9).

[3] W.S. Sanders, L.J. Gibson, Mechanics of BCC and FCC hollow-sphere foams, *Mater. Sci. Eng. A* 352 (2003) 150–161, [https://doi.org/10.1016/S0921-5093\(02\)00890-0](https://doi.org/10.1016/S0921-5093(02)00890-0).

[4] T.J. Lim, B. Smith, D.L. McDowell, Behavior of a random hollow sphere metal foam, *Acta Mater.* 50 (2002) 2867–2879, [https://doi.org/10.1016/S1359-6454\(02\)00111-8](https://doi.org/10.1016/S1359-6454(02)00111-8).

[5] O. Caty, E. Maire, R. Bouchet, Fatigue of metal hollow spheres structures, *Adv. Eng. Mater.* 10 (2008) 179–184, <https://doi.org/10.1002/adem.200700265>.

[6] H.H. Ruan, Z.Y. Gao, T.X. Yu, Crushing of thin-walled spheres and sphere arrays, *Int. J. Mech. Sci.* 48 (2006) 117–133, <https://doi.org/10.1016/j.ijmesci.2005.08.006>.

[7] S.T. Szymiszewski, B.H. Smith, J.F. Hajjar, B.W. Schafer, S.R. Arwade, The mechanical properties and modeling of a sintered hollow sphere steel foam, *Mater. Des.* 54 (2014) 1083–1094, <https://doi.org/10.1016/j.matdes.2013.08.045>.

[8] W.S. Sanders, L.J. Gibson, Mechanics of hollow sphere foams, *Mater. Sci. Eng. A* 347 (2003) 70–85, [https://doi.org/10.1016/S0921-5093\(02\)00583-X](https://doi.org/10.1016/S0921-5093(02)00583-X).

[9] M. Koopman, G. Gouadec, K. Carlisle, K.K. Chawla, G. Gladysz, Compression testing of hollow microspheres (microballoons) to obtain mechanical properties, *Scr. Mater.* 50 (2004) 593–596, <https://doi.org/10.1016/j.scriptamat.2003.11.031>.

[10] S. Gasser, F. Paun, A. Cayzele, Y. Bréchet, Uniaxial tensile elastic properties of a regular stacking of brazed hollow spheres, *Scr. Mater.* 48 (2003) 1617–1623, [https://doi.org/10.1016/S1359-6462\(03\)00139-8](https://doi.org/10.1016/S1359-6462(03)00139-8).

[11] K.B. Carlisle, M. Lewis, K.K. Chawla, M. Koopman, G.M. Gladysz, Finite element modeling of the uniaxial compression behavior of carbon microballoons, *Acta Mater.* 55 (2007) 2301–2318, <https://doi.org/10.1016/j.actamat.2006.11.026>.

[12] K.B. Carlisle, M. Koopman, K.K. Chawla, R. Kulkarni, G.M. Gladysz, M. Lewis, Microstructure and compressive properties of carbon microballoons, *J. Mater. Sci.* 41 (2006) 3987–3997, <https://doi.org/10.1007/s10853-006-7574-8>.

[13] N. Gupta, G. Easwara Prasad, S. Gupta, Axial compression of metallic spherical shells between rigid plates, *Thin-Walled Struct.* 34 (1999) 21–41, [https://doi.org/10.1016/S0263-8231\(98\)00049-4](https://doi.org/10.1016/S0263-8231(98)00049-4).

[14] N.K. Gupta, Venkatesh, Experimental and numerical studies of dynamic axial compression of thin walled spherical shells, *Int. J. Impact Eng.* 30 (2004) 1225–1240, <https://doi.org/10.1016/j.ijimpeng.2004.03.009>.

[15] G.L.E. Prasad, N.K. Gupta, An experimental study of deformation modes of domes and large-angled frusta at different rates of compression, *Int. J. Impact Eng.* 32 (2005) 400–415, <https://doi.org/10.1016/j.ijimpeng.2004.12.001>.

[16] X.L. Dong, Z.Y. Gao, T.X. Yu, Dynamic crushing of thin-walled spheres: an experimental study, *Int. J. Impact Eng.* 35 (2008) 717–726, <https://doi.org/10.1016/j.ijimpeng.2007.11.004>.

[17] P. Li, N. Petrinic, C.R. Siviour, Finite element modelling of the mechanism of deformation and failure in metallic thin-walled hollow spheres under dynamic compression, *Mech. Mater.* 54 (2012) 43–54, <https://doi.org/10.1016/j.mechmat.2012.06.002>.

[18] A.P. Roberts, E.J. Garboczi, Elastic properties of model porous ceramics, *J. Am. Ceram. Soc.* 83 (2000) 3041–3048, <https://doi.org/10.1111/j.1151-2916.2000.tb01680.x>.

[19] J. Song, Q. Sun, Z. Yang, S. Luo, X. Xiao, S.R. Arwade, G. Zhang, Effects of microporosity on the elasticity and yielding of thin-walled metallic hollow spheres, *Mater. Sci. Eng. A* 688 (2017) 134–145, <https://doi.org/10.1016/j.msea.2017.01.105>.

[20] A. Fallet, P. Lhuissier, L. Solvo, Y. Bréchet, Mechanical behaviour of metallic hollow spheres foam, *Adv. Eng. Mater.* 10 (2008) 858–862, <https://doi.org/10.1002/adem.200800094>.

[21] Y. Liu, H.X. Wu, B. Wang, Gradient design of metal hollow sphere (MHS) foams with density gradients, *Compos. Part B Eng.* 43 (2012) 1346–1352, <https://doi.org/10.1016/j.compositesb.2011.11.057>.

[22] S. Aghajari, K. Abedi, H. Showkati, Buckling and post-buckling behavior of thin-walled cylindrical steel shells with varying thickness subjected to uniform external pressure, *Thin-Walled Struct.* 44 (2006) 904–909, <https://doi.org/10.1016/j.tws.2006.08.015>.

[23] M. Shariati, H.R. Allahbakhsh, Numerical and experimental investigations on the buckling of steel semi-spherical shells under various loadings, *Thin-Walled Struct.* 48 (2010) 620–628, <https://doi.org/10.1016/j.tws.2010.03.002>.

[24] W. Wunderlich, U. Albertin, Buckling behaviour of imperfect spherical shells, *Int. J. Non Linear Mech.* 37 (2002) 589–604, [https://doi.org/10.1016/S0020-7462\(01\)00086-5](https://doi.org/10.1016/S0020-7462(01)00086-5).

[25] A. Szlancsik, B. Katona, K. Bobor, K. Májlinger, I.N. Orbulov, Compressive behaviour of aluminium matrix syntactic foams reinforced by iron hollow spheres, *Mater. Des.* 83 (2015) 230–237, <https://doi.org/10.1016/j.matdes.2015.06.011>.

[26] G. Zhang, H. Yin, A. Reed, Nanomechanical characterization of clay micro flocs, *Soc. Eng. Sci. 51st Annu. Tech. Meet.* 2014.

[27] Z. Zhang, Z. Wei, R. Ferrell, Elastic modulus and hardness of muscovite and rectorite determined by nanoindentation, *Appl. Clay Sci.* 43 (2009) 271–281, <https://doi.org/10.1016/j.clay.2008.08.010>.

[28] W.C. Oliver, G.M. Pharr, An improved technique for determining hardness and elastic modulus using load and displacement sensing indentation experiments, *J. Mater. Res.* 7 (1992) 1564–1583, <https://doi.org/10.1557/JMR.1992.1564>.

[29] J. Menčík, D. Munz, E. Quandt, E.R. Weppelmann, M.V. Swain, Determination of elastic modulus of thin layers using nanoindentation, *J. Mater. Res.* 12 (1997) 2475–2484, <https://doi.org/10.1557/JMR.1997.0327>.

[30] M. Dao, N. Chollacoop, K.J. Van Vliet, T.A. Venkatesh, S. Suresh, Computational modeling of the forward and reverse problems in instrumented sharp indentation, *Acta Mater.* 49 (2001) 3899–3918, [https://doi.org/10.1016/S1359-6454\(01\)00295-6](https://doi.org/10.1016/S1359-6454(01)00295-6).